Proximity proteomics reveals UCH-L1 as an NLRP3 interactor that modulates IL-1β production in human macrophages and microglia

Zhu Liang[1,2,12*], Andreas Damianou[1,2,12], Iolanda Vendrell[1,2], Edward Jenkins[3], Frederik H. Lassen[4], Sam J Washer[5,6], Guihai Liu[1], Gangshun Yi[7], Hantao Lou[8], Fangyuan Cao[9], Xiaonan Zheng[1], Ricardo A. Fernandes[1], Tao Dong[1], Edward W. Tate[9], Elena Di Daniel[10,11], Benedikt M Kessler[1,2*]

[1]Chinese Academy for Medical Sciences Oxford Institute, Nuffield Department of Medicine, University of Oxford, Roosevelt Drive, Oxford OX3 7FZ, UK

[2]Target Discovery Institute, Centre for Medicines Discovery, Nuffield Department of Medicine, University of Oxford, Roosevelt Drive, Oxford OX3 7FZ, UK

[3]Kennedy Institute of Rheumatology, University of Oxford, OX3 7FY UK

[4]Big Data Institute, Li Ka Shing Centre for Health Information and Discovery, Nuffield Department of Medicine, University of Oxford, Old Road Campus OX3 7LF, UK

[5]James and Lillian Martin Centre for Stem Cell Research, Sir William Dunn School of Pathology, University of Oxford, South Parks Road, Oxford, OX1 3RE, UK

[6]Wellcome Centre for Human Genetics, Nuffield Department of Medicine, University of Oxford, Oxford, UK

[7]Division of Structural Biology, Wellcome Trust Centre for Human Genetics, University of Oxford, Oxford OX3 7BN, UK

[8]Ludwig Institute for Cancer Research, University of Oxford, Oxford, UK

[9]Department of Chemistry, Molecular Sciences Research Hub, Imperial College London, London, W12 0BZ, UK

[10]Alzheimer's Research UK Oxford Drug Discovery Institute, University of Oxford, Oxford OX3 7FZ, United Kingdom

[11]Present address: Astex Pharmaceuticals, 436 Cambridge Science Park, Milton Rd, Milton, Cambridge CB4 0QA, UK

[12]Equal contribution

Running title: UCH-L1 regulates NLRP3 inflammasome & IL-1β production

***Corresponding author(s):** Zhu Liang, email: zhu.liang@ndm.ox.ac.uk

Benedikt M Kessler, email: benedikt.kessler@ndm.ox.ac.uk

Key words: Deubiquitylase, DUB, IL-1β, inflammasome, NLRP3, protease inhibitor, ubiquitin, UCH-L1

ABSTRACT (149 words)

Activation of the NACHT, LRR family pyrin domain containing 3 (NLRP3) inflammasome complex is an essential innate immune signalling mechanism. To reveal how human NLRP3 inflammasome assembly and activation are controlled, in particular by components of the ubiquitin system, proximity labelling, affinity purification and RNAi screening approaches were performed. Our study provides an intricate time-resolved molecular map of different phases of NLRP3 inflammasome activation. Also, we show that ubiquitin C-terminal hydrolase 1 (UCH-L1) interacts with the NACHT domain of NLRP3. Downregulation of UCH-L1 decreases pro-IL-1β levels. UCH-L1 chemical inhibition with small molecules interfered with NLRP3 puncta formation and ASC oligomerization, leading to altered IL-1β cleavage and secretion, particularly in microglia cells, which exhibited elevated UCH-L1 expression as compared to monocytes/macrophages. Altogether, we profiled NLRP3 inflammasome activation dynamics and highlight UCH-L1 as an important modulator of NLRP3-mediated IL-1β production, suggesting that a pharmacological inhibitor of UCH-L1 may decrease inflammation-associated pathologies.

INTRODUCTION

Innate immunity reflects a cornerstone of defence systems in living organisms which integrates with adaptive immune responses in the case of higher eukaryotes (Paludan et al., 2021). A major hallmark is the activation of inflammasome complexes, composed of ASCs and NLRs, such as NACHT, LRR family pyrin domain containing 3 (NLRP3) (Martinon et al., 2002) involving cleavage of pro-IL1β by caspase-1 (Gross et al., 2012). External stimuli including lipopolysaccharide (LPS) as the first, and nigericin, monosodium urate (MSU) monohydrate, Alum, ATP or cholesterol crystals as the second signal lead to the assembly and activation of the NLRP3 inflammasome complex, resulting in inflammatory responses (Shao et al., 2015; Swanson et al., 2019). Assembly of this supramolecular structure, featuring NLRP3 and ASC, is further regulated by associated factors, such as NEK7 (He et al., 2016), as well as specific posttranslational modifications including phosphorylation and ubiquitylation (Akther et al., 2021; Liang et al., 2021; Zangiabadi and Abdul-Sater, 2022). In addition to the kinases RIPK3 (Lawlor et al., 2015), FYN (Panicker et al., 2019) and ubiquitin ligases TRIM31(Song et al., 2016), gp78/Insig-1 (Xu et al., 2022), MARCH7 (Yan et al., 2015), HUWE1 (Guo et al., 2020), RNF25 and Cbl (Tang et al., 2020), deubiquitylases (DUBs) have been shown to modulate ubiquitylation of components of the inflammasome often in the context of specific diseases (Lopez-Castejon, 2020; Lopez-Castejon and Edelmann, 2016; Lopez-Castejon et al., 2013). More specifically, ubiquitylation and deubiquitylation of NLRP3 and IL-1β (Vijayaraj et al., 2021) have been reported to reflect critical checkpoints of NLRP3 inflammasome complex assembly, activation and signalling (Lopez-Castejon, 2020; Lopez-Castejon and Edelmann, 2016; Lopez-Castejon et al., 2013). Ubiquitin protease 7 (USP7) and 47 (USP47) inhibition resulted in reduced inflammasome activation (Palazon-

69 Riquelme et al., 2018). In addition, in mice, BRCC3, a DUB reflecting a component of the BRISC
70 complex, was shown to deubiquitylate NLRP3, thereby regulating inflammasome activity (Py et al.,
71 2013). Recently, increasing number of findings suggest a complex interplay between ubiquitylation and
72 deubiquitylation mechanisms that modify components of the inflammasome complex. However, most
73 studies of ubiquitin-mediated NLRP3 pathway were conducted in murine models, such as NG5, mouse
74 peritoneal macrophages, and mouse bone marrow-derived macrophages (BMDMs) (Py et al., 2013; Ren
75 et al., 2019; Song et al., 2020). Given the inter-species divergence between human and mouse
76 inflammasome complexes and regulatory pathways, the role of ubiquitylation/deubiquitylation in
77 human NLRP3 inflammasome activation remains largely unknown.

78 To gain a more comprehensive understanding of the ubiquitin-mediated regulation of the human
79 NLRP3 inflammasome, we have combined ascorbic acid peroxidase 2 (APEX2)-based proximity
80 labelling, affinity purification and RNAi screening to discover molecular factors involved in the primary
81 and secondary signals of NLRP3 inflammasome activation and assembly. In both, a reconstituted
82 system and macrophages, we demonstrate that UCH-L1 interacts with the NACHT domain of NLRP3
83 and thereby interferes with ASC and NLRP3 assembly. Furthermore, ubiquitin C-terminal hydrolase 1
84 (UCH-L1) knockdown or chemical inhibition interferes with IL-1β production, particularly in microglia
85 cells that exhibited elevated UCH-L1 expression as compared to peripheral monocytes or macrophages.

86 **RESULTS**

87 **NLRP3-APEX2 captures the NLRP3 molecular proximity network**

88 As the N-terminus NLRP3 PYD domain has been reported to be responsible for initiating NLRP3
89 oligomerization, we inserted APEX2 at the C-terminus (LRR domain) of NLRP3 including a flexible
90 linker between these domains and a flag epitope at the N-terminus (**Figure 1A**). To avoid unstable
91 expression and mis-localization during transient transfection, we generated a NLRP3-APEX2 HEK293
92 stable cell line using the Flp-In T-REx system, allowing dose-dependent control of expression with
93 tetracycline (**Figures S1A, B**). Fluorescence microscopy confirmed that both flag-NLRP3 and flag-
94 NLRP3-APEX2 can form puncta in the perinuclear areas in response to nigericin stimulation, while the
95 fusion proteins are diffused across the cytosol in the resting state (**Figures S1C, D**). ASC
96 oligomerization assays with co-expression of adaptor protein ASC in stable cell lines proved that both
97 flag-NLRP3 and flag-NLRP3-APEX2 are competent to recruit ASC and induce its polymerization upon
98 stimulation with nigericin (**Figures S2A, B**). Taken together, these results indicate that APEX2 tagging
99 fused to the C-terminus of NLRP3 does not impede its ability to sense stimuli, particularly nigericin
100 induced potassium efflux, and recruit ASC to form oligomers.

101 We next investigated whether biotin labelling profiles are spatially restricted to the fusion bait. Live
102 HEK293 cells expressing NLRP3-APEX2 were treated with or without nigericin. Subsequently, cells

103 were treated with H_2O_2 in the presence of biotin-phenol, followed by rapid quenching, methanol fixation
104 and staining (**Figure 1B**). In contrast to the native control without H_2O_2 treatment, we observed robust
105 biotinylation by streptavidin-Alexa Fluor 488 imaging. Under unstimulated conditions, NLRP3-APEX2
106 was diffused across the cytosol, with biotinylated proteins following similar distribution pattern. Upon
107 nigericin treatment, NLRP3-APEX2 oligomerized to form puncta close to the nucleus, and we also
108 observed specks formed by biotin labelled proteins (**Figure 1C**). This partially suggests the spatial
109 specificity of NLRP3-APEX2 induced biotinylation.

110 The ability of APEX2 to efficiently label and capture the NLPR3 "proximitome" was assessed using
111 streptavidin immunoblotting and Coomassie blue staining, confirming the robust biotin labelling
112 activity of APEX2 fused to NLRP3 (**Figure 1D, Figure S3B**). Initially, we investigated whether
113 APEX2 is competent to capture the known NLRP3-interacting protein-NIMA-related kinase 7 (NEK7).
114 In contrast to the unlabelled negative control, we found that NLRP3-APEX2 specifically biotinylated
115 NEK7. Additionally, a substantial increase in NEK7 protein sequestration was observed in association
116 with activated NLRP3 (**Figure 1D**).

117 Given the rapid kinetic properties of APEX2 proximity labelling, we next sought to map the
118 spatiotemporally resolved "proximitome" of NLRP3 upon stimulation by nigericin across various time
119 intervals. Following mass spectrometric analysis, 3,478 proteins in total were detected across the
120 DMSO control and nigericin treatment for 30 min, 60 min and 90 min. To maximize the signal-to-noise
121 ratio and discriminate the bona fide interacting partners from the background contaminants, Bayesian
122 model-based algorithm SAINTexpress (Teo et al., 2014) was applied, yielding 800-1,100 high
123 confidence NLRP3 proximal proteins (**Figures 2A-B, Figure S3A**). Unsupervised principal component
124 analysis (PCA) showed the clustering and patterns of different protein subgroups (**Figure 2C**). High
125 correlation was observed between the three biological repeats within each group confirming the low
126 technical variation in this experiment (**Figure S3C**).

127 To assess the specificity of the NLRP3 proximity proteome, we next sought to check if the known
128 NLRP3 interactors or regulators are biotinylated and captured by APEX2. SAINT probability scoring
129 and simpler fold-change (FC) were calculated by the comparison of prey protein abundance between
130 the bait and negative beads control. Previously reported 83 human NLRP3 interactors, retrieved from
131 public interaction repository BioGrid (https://thebiogrid.org/, version 4.4.209) and the literature (**Table**
132 **S1**) (Oughtred et al., 2021; Oughtred et al., 2019; Stark et al., 2006) were mapped and plotted with
133 stringent thresholds (SAINT probability > 0.8, FC-A ≥ 1). After filtering, 14 known NLRP3 interactors
134 (16%) were discerned as high-confidence hits within the proximal proteomic data (**Figures 2D-H,**
135 **Figure S4**) confirming the enrichment of NLRP3-associated proteins.

136 **Temporal tracking of the NLRP3 proximity proteome**

137 To gain mechanistic and functional insights into the NLRP3 proximity proteome following nigericin
138 stimulation at various intervals, we conducted a gene ontology-biological process (GO term-BP)
139 enrichment analysis (**Figure 2I**). 13 shared terms, including viral translation, apoptotic cell death
140 regulation, stress granule assembly and mitosis-associated processes, were significantly enriched across
141 all four groups. In contrast to the unstimulated control, pathways related to "protein kinase D signalling"
142 and "mRNA binding regulation" were uniquely present after nigericin-exposure, consistent with prior
143 observations (Zhang et al., 2017). Intriguingly, the enrichment of "cellular response to arsenite ion" and
144 "regulation of stress granule disassembly" terms suggest a potential functional association between
145 inflammasome and stress granule formation. This connection was substantiated by previous reports of
146 the stress granule protein DDX3X as a pivotal mediator, modulating between apoptotic ASC speck
147 formation and pro-survival stress signalling (Fox and Man, 2019; Samir et al., 2019). In terms of GO
148 term-molecular function (GO term-MF) enrichment analysis, "GTP-dependent protein binding" and "1-
149 phosphatidylinostitol binding" were significantly enriched solely in the nigericin-60 min and nigericin-
150 90 min groups, suggesting that nigericin treatment might induce the recruitment of proteins associated
151 with the above two biological functions (**Figures S5A-C**). GO term-cellular components (CC) analysis
152 identified 16 common subcellular compartments or complexes, including COPII vesicle coat, ESCRT-
153 0 complex, and chaperone complex. Notably, three endocytic recycling-associated complexes,
154 including the endosome-associated recycling protein (EARP) complex, endosome to plasma transport
155 vesicle and Golgi-associated retrograde protein (GARP) complex, were significantly enriched solely in
156 nigericin-60 min and nigericn-90 min groups, suggesting that the NLRP3 complex may translocate to
157 trans-Golgi network (TGN) or endosome upon stimulation (**Figure S5D**). Similarly, the compartments
158 enrichment analysis identified another four complexes, including Dcp1-Dcp2, signal recognition
159 receptor, MAD1 and the cohesin I complex, which were only captured and enriched in the last two
160 timepoints of nigericin treatment (**Figures S6A-E**). We also performed tissue enrichment analysis, and
161 not surprisingly, poor tissue specificity was observed in either unstimulated or stimulated groups
162 (**Figure S5E**). To further explore the physiological and pathological biological processes, a reactome
163 pathway analysis was performed on the proximity proteome. The top 20 significantly enriched pathways
164 are shown as in **Figure S6F**. Notably, several innate immunity and virus infection associated pathways,
165 such as interleukin-6 signalling, MHC class I complex, and PP2A-mediated dephosphorylation of key
166 metabolic factors, were identified and enriched. Selected gene sets involved in the above pathways are
167 plotted in **Figures S6G-H**.

168 **Localization analysis reveals translocation of NLRP3 upon stimulation**

169 As the subcellular relocalization of NLRP3 and its underlying mechanism remain controversial
170 (Hamilton and Anand, 2019), we performed the localization analysis to assess the spatial properties of
171 NLRP3 inflammasome during complex assembly. After the filtering, normalization, and imputation,
172 we compared the relative abundance of biotinylated proteins in the unstimulated (DMSO) and

173 stimulated states (nigericin-90 min). The resulting volcano plot (**Figure S3F**) shows 103 proteins
174 enriched in the right quadrant for the stimulated state, while 104 proteins enriched in the left quadrant
175 for the resting state, with relatively stringent cut-off for fold change and false discovery rate
176 (log2[FC]≥0.5 or ≤-0.5, FDR≤ 0.05). GO term-CC enrichment analysis was performed on the
177 differentially enriched proteins in either condition. The proximity proteome under stimulated condition
178 showed high spatial specificity for Golgi apparatus, with 24 proteins falling into the GO-CC term
179 category-Golgi membranes (**Figures S3D-F, Table S2**). This is consistent with the previous
180 observation that NLRP3 is activated and recruited to dispersed trans-Golgi networks (dTGN) in
181 response to diverse stimuli (Bordon, 2019; Chen and Chen, 2018).

182 **Mapping stimulation-dependent NLRP3 interaction alterations using APEX2-PL and AP-MS**

183 Modulation of the NLRP3 local milieu during the activation process was further examined using an
184 integrated approach that combined NLRP3 APEX2 proximity labelling (PL) and affinity purification
185 mass spectrometry (AP-MS) (**Figure 3A**). For APEX2 PL-MS, the SAINTexpress analysis identified
186 848 (DMSO) and 833 (Nig-90min) proximal proteins, while 484 (DMSO) and 366 potential interacting
187 proteins were captured using the AP-MS method (**Figures 3A, B, Figures S7A-H**). There was relatively
188 small number of overlapping proteins between APEX2 and AP-MS possibly as a result of the
189 complementary nature of these two techniques (**Figures 3C, D**) and consistent with previous studies
190 comparing BioID and AP-MS (Lambert et al., 2015). Additionally, we sought to compare the proximal
191 proteome of NLRP3 under both resting and activation states. Following a rigorous filtration, seven
192 known NLRP3-interacting proteins were differentially enriched. Of these, five proteins (NEK7, MAVS,
193 PRKD1, PRKD2, and PRKD3, highlighted in red) enriched in the right quadrant are established positive
194 regulators of NLRP3. In contrast, EIF2AK2 and LYN (highlighted in green) in the left quadrant are
195 previously characterized inhibitory mediators. Interestingly, we noticed an increased labelling and
196 capture of NLRP3 under stimulated conditions, likely due to oligomerization (**Figure 3E**).

197 To gain a visual understanding of the interaction networks within the NLRP3 proximity proteome and
198 infer related biological insights, we performed a PPI network analysis. As for the nigericin stimulated
199 condition (**Figure 3F)**, we identified protein complexes including the NLRP3 inflammasome, NEK7,
200 MAVS, the SNARE complex, COPII vesicle coat, the signal recognition particle receptor complex and
201 the protein kinase D signalling complex. **Figure 3G** highlights the interaction networks linked to the
202 unstimulated state, in which the centrosome, the catenin complex, translational initiation factor, calcium
203 dependent serine kinase and the N-end rule proteasomal pathway were significantly enriched.

204 **NLRP3-associated DUBs identified by proximity proteome-guided RNAi screening**

205 The proximity proteome enabled us to capture several ubiquitin system components including 18 DUBs
206 in total (USP9X, USP8, USP5, USP47, USP32, USP24, USP19, USP15, USP14, USP10, USP1, UCH-
207 L1, PAN2, OTULIN, OTUID4, OTUB1, EIF3H and CYLD), which passed the stringent filtering criteria

208 (SAINT probability > 0.8, FC-A ≥ 1). Among the 18 enriched DUBs, 9 were consistently present in all
209 the four groups, and no marked difference was noted between the stimulated and unstimulated states
210 (**Figures 4A-E**). To complement this, we carried out a DUB library RNAi screen in PMA-differentiated
211 THP-1 cells, aiming to assess their influences on NLRP3 inflammasome priming and activation,
212 reflected by IL-1β production. In total, knockdown of 25 DUBs (outliers that surpass mean ± 1 standard
213 deviation, z score ≥1 or ≤-1, **Table S3**) were found to alter IL-1β levels in THP-1 cells treated with LPS
214 or LPS /nigericin (**Figures 4F-G**). A combination of proximity proteomics and RNAi screening revealed
215 7 DUBs showing effects in both assays (USP9X, USP8, USP14, USP10, UCH-L1, OTUB1 and OTUD4)
216 (**Figure 4H**). USP9X, USP14, and OTUB1 have already been reported to modulate the NLRP3
217 inflammasome (Hai et al., 2022; Xiang et al., 2023), suggesting additional NLRP3-associated DUBs
218 (USP8, USP10, OTUD4 and UCH-L1).
219

220 **UCH-L1 interacts with the NACHT domain of NLRP3 and affects IL-1β production**

221 Amongst these DUBs, UCH-L1 consistently affected IL-1β levels and showed high NLRP3 proximity
222 scores. Notably, the knockdown of UCH-L1 did not alter pro-IL-1β mRNA expression, while it
223 decreased protein levels and production of the mature form in THP-1 monocytes (**Figures 4I, J**) and
224 human PBMCs (**Figures 4K, L**). Expression of IL-6 and TNFα were also slightly suppressed in the
225 absence of UCH-L1 (**Figure S8B, C**), indicating that UCH-L1 might also play a role in the NF-κB-
226 regulated priming stage. As UCH-L1 is highly abundant in cells associated with the central nervous
227 system, we sought to investigate its role in brain resident immune cells, such as microglia, which also
228 express NLRP3 inflammasome components (**Figure S9**). Similarly to THP-1 and PBMC cells, UCH-
229 L1 deficiency markedly suppressed IL-1β production in the human microglial cell line HMC3 (**Figures**
230 **4M, N**).
231

232 The NLRP3-UCH-L1 interaction was identified through NLRP3-APEX2 proximity labelling (**Figure**
233 **5A**) and confirmed by immunoprecipitation (**Figure 5B**) in HEK293 cells. Notably, the interaction
234 between NLRP3 and UCH-L1 decreases upon nigericin stimulation (**Figure 5B**). To further determine
235 which domain within NLRP3 interacts with UCH-L1, we overexpressed flag-tagged full-length and
236 truncated NLRP3 in HEK293T cells. UCH-L1 interacted with the full-length NLRP3 and NACHT
237 domain of NLRP3 (**Figure 5C**). These results imply that the NACHT domain of NLRP3 directly or
238 indirectly provides a binding site for UCH-L1. Additionally, immunofluorescence revealed the
239 colocalization of NLRP3 with UCH-L1 in hiPSC-derived microglial cells (**Figures 5D, E**).
240

241 **UCH-L1 catalytic inhibition abrogates ASC assembly, NLRP3 inflammasome activation and IL-**
242 **1β processing**

243 To investigate how UCH-L1 modulates IL-1β processing and release, we selected a potent inhibitor-
244 IMP-1711-S (small molecule 27 in patent (Mark Kemp, 2017), **Figure 6A**) (Panyain et al., 2020;
245 Panyain et al., 2021) and tested its effect on NLRP3 inflammasome activation in THP-1, mouse bone
246 marrow-derived macrophages (BMDMs), human PBMCs, and hiPSC-derived microglial cells. Cells
247 were primed with LPS, pre-treated with IMP-1711-S and stimulated with the NLRP3 activator nigericin.
248 We observed that the treatment with IMP-1711-S inhibited the production of IL-1β in a concentration-
249 dependent manner in PMA-differentiated THP-1 (**Figure 6B**) and hiPSC-derived microglia (**Figures**
250 **6K, L**). Both, caspase-1 p10 and cleaved IL-1β levels were reduced in supernatants from IMP-1711-S-
251 treated THP-1 cells (**Figures 6C-E**), suggesting that the inhibitor exerts its effect on the activation of
252 the caspase-1 and IL-1β processing stage. IMP-1711-S potently inhibited the release of lactate
253 dehydrogenase (LDH) and blocked pyroptotic cell death induced by nigericin (**Figures 6F, G**).
254 Additionally, IMP-1711-S treatment did not affect pro-caspase-1 or pro-IL-1β expression in lysates in
255 the priming stage with LPS stimulation (**Figure 6C**). Further investigation of ASC oligomerization in
256 THP-1 cells through crosslinking of the insoluble lysate fraction revealed that while IMP-1711-S had
257 no impact on ASC expression in cell lysates, it substantially reduced oligomerized ASC levels post LPS
258 and nigericin stimulation (**Figure 6H**). Additionally, in HEK293 cells, IMP-1711-S markedly
259 downregulated the formation of NLRP3 specks in a concentration-dependent manner (**Figures 6I, J**).
260 Our findings underscore that UCH-L1 inhibition impedes NLRP3 inflammasome activation by
261 disrupting NLRP3 assembly and the speck formation, ultimately leading to decreased IL-1β production
262 (**Figure 7**).
263

264 ## DISCUSSION

265 The NLRP3 inflammasome is central to innate immunity, and a detailed understanding of its molecular
266 dynamics and interactome is highly sought after. We found that NLRP3 tolerates C-terminally tagged
267 APEX2, retaining its competence to biotinylate and capture known interacting partners of endogenous
268 NLRP3. Using complementary techniques, such as APEX2 PL-MS, AP-MS, and siRNA screening, we
269 traced the time-resolved PPI networks local to the NLRP3 inflammasome upon stimulation. This
270 approach offers a resource-rich map for further investigations of the molecular intricacies of NLRP3
271 inflammasome activation and revealed that UCH-L1 is involved in regulating IL-1β production.

272 ### Deconvolution of the NLRP3-APEX2 proximity proteome

273 A critical issue related to proximity labelling experiments is discrimination between true interactors and
274 background noise. Proteins captured by NLRP3-APEX2 proximity labelling can be categorized into four
275 groups: Type I-True interacting proteins that physically interact with NLRP3 and or other components
276 of the complex; Type II-Compartmental or proximal proteins in the local milieu of NLRP3 reflecting
277 transient interactions; Type III-non-specific proteins that stick to streptavidin beads; Type IV-physically
278 non-existing proteins detected in error. Type I and type II provide insights into the PPI network and

279 local milieu of NLRP3, but type III and type IV are considered false positives. To establish a high
280 confidence proximity proteome resource for NLRP3, a variety of approaches were used to filter out type
281 III and type IV contaminant proteins. A Bayesian model-based algorithm (SAINTexpress) was applied
282 to analyze the proximity labelling data with a SAINT probability score threshold of 0.8 and fold change
283 ≥ 2, yielding 800-1100 proximal proteins per group (**Figures 2C, E-H**). Furthermore, the unstimulated
284 state was used as a control, which helped us distinguishing the differentially regulated interacting
285 partners upon stimulation with nigericin, still yielding more than 800 proteins per biological condition,
286 consistent with the APEX2 enzyme affording a biotin labelling radius of ~ 10 nm in live cells (Qin et
287 al., 2021). With a stringent cut-off, our data identified 103 high-confidence putative NLRP3-associated
288 proteins enriched under activated conditions and 104 proteins enriched under inactivated conditions.
289 These included known interactors, such as NEK7, MAVS, PRKD1/2/3, LYN and EIF2AK2 (**Figure**
290 **3E**). We note that spatial references have been shown to enhance the deconvolution of PL data. However,
291 in our study, this was not applied as NLRP3 resides in multiple compartments and translocates to distinct
292 organelles upon activation (Hamilton and Anand, 2019). By integrating PL data with AP-MS and siRNA
293 screening, we established an alternative method for validating NLRP3-associated proteins.
294

295 **UCH-L1 is an essential mediator of NLRP3/ASC assembly and IL-1β production**

296 Ubiquitin modification controls multiple elements of the NLPR3 activation process and IL-1β
297 production (Lopez-Castejon, 2020). Through a DUB siRNA screen, we pinpointed four deubiquitylating
298 enzymes, TNFAIP3, CYLD, USP7, and STAMBP, already been linked to IL-1β signalling pathways
299 (**Figure 4G)** (Bednash et al., 2021; Duong et al., 2015; Palazon-Riquelme et al., 2018; Vande Walle et
300 al., 2014; Yang et al., 2020). However, the intricate nature of IL-1β processing, spanning multiple
301 regulatory stages, poses a challenge to precisely attribute the functional impacts of each DUB. For
302 instance, UCH-L3 and L5 were suggested to affect inflammasome activation and IL-1β production,
303 although in the context of infection (Kummari et al., 2015; Qu et al., 2020; Ramachandran et al., 2021).
304 UCH-L3 may act in the priming stage, whereas UCH-L5's role maybe less clear outside the context of
305 pathogen-driven NLRP3 inflammasome activation, consistent with the former, but not the latter, being
306 detected in our screen (**Fig. 4G**).
307 Here, we identified UCH-L1 as an NLRP3 interacting modulator of the inflammasome. It is a member
308 of the ubiquitin C-terminal hydrolase (UCH) family involved in neurodegeneration and cancer
309 metastasis (Ham et al., 2021; Liu et al., 2002; Mondal et al., 2022b). UCH-L1 is highly expressed in the
310 central nervous system, with low expression levels in most other tissues under normal physiology.
311 Dysregulation of UCH-L1 expression and mutations have been implicated in multiple
312 neurodegenerative diseases, such as Parkinson's disease, Huntington's disease, and recessive hereditary
313 spastic paraplegia (SPG79) (Mondal et al., 2022a). Also, several studies linked UCH-L1 to inflammation
314 or innate immunity. For instance, UCH-L1 deficiency markedly reduces the secretion of pro-

315 inflammatory cytokines, notably IL-6 and TNFα (Zhang et al., 2021). LDN57444, an isatin O-acyl
316 oxime small molecule inhibitor, has demonstrated efficacy in ameliorating LPS-induced sepsis in *in vivo*
317 models (Zhang et al., 2021), although other studies have cast doubt on the specificity or efficacy of this
318 compound against UCH-L1 (Panyain et al., 2020). Another study reported that UCH-L1 promoted M1
319 macrophages polarization via the PI3K/Akt signalling pathway (Huang et al., 2022). Consistent with
320 previous findings, UCH-L1 knockdown or inhibition yielded a significant decrease in pro-inflammatory
321 cytokine expression and secretion including IL-1β, IL-6 and TNFα in both, THP-1 and human primary
322 monocytes, reflecting interference in upstream signalling affecting the priming stage (**Figures 4I-L,**
323 **Figures S8, S10**). Furthermore, mRNA levels of IL-1β remain unchanged in the absence of UCH-L1,
324 suggesting that UCH-L1 affects IL-1β at the post-transcriptional or protein level (**Figure 4J**). Notably,
325 pharmacological inhibition of UCH-L1 affected ASC/NLRP3 assembly and IL-1β production, which
326 are part of the second inflammasome induction signal (**Figure 6**). Although the small molecule inhibitor
327 IMP-1711-S altered secreted active caspase-1 levels (**Figure 6E**), it does not seem to cross-react or
328 inhibit caspases directly (Panyain et al., 2020). Caspase-1 inhibitors also show a different specificity
329 profile towards TNFα release (Cao et al., 2022). UCH-L1 inhibition interferes with upstream events,
330 such as NLRP3 puncta formation and ASC oligomerization (**Figure 6**), the latter of which is
331 phenocopied by UCH-L1 knockdown (**Figure S11**). UCH-L1, found to be bound to the NACHT domain
332 of NLRP3, may act as a gating/editing factor to control the ubiquitylation status of multiple components,
333 such as NLRP3, ASC, Caspase-1 and IL-1β, required for NLRP3-ASC inflammasome complex
334 assembly (**Figure 7**). Preliminary results indicate that NLRP3's half-live is dependent on the ubiquitin-
335 proteasome pathway (**Figure S12**). However, NLRP3 associated ubiquitylation appears to be minimally
336 altered by UCH-L1, and NLRP3 protein levels are unaffected (**Figures S12, 13**), suggesting a more
337 structural role for UCH-L1 and/or its modulation of NLRP3 ubiquitination during assembly rather than
338 controlling turnover. Though speculative at this stage, such a putative structural and ubiquitylation
339 editing "gate keeping" process maybe in analogy to the role of UCH-L5/UCH37 in the 26S proteasome
340 complex, required for substrate deubiquitylation and ubiquitin recycling prior to substrate unfolding by
341 the 19S and entry into the 20S for destruction (Song et al., 2021; Vander Linden et al., 2015).
342
343 In conclusion, in this study, we provide a detailed NLRP3 inflammasome interaction map at different
344 physiological stages. UCH-L1 was identified and validated as an essential regulator involved in NLRP3
345 inflammasome activation and IL-1β production, affected by UCH-L1 chemical inhibition and
346 phenocopied by UCH-L1 deletion. Our results may have translational implications in exploring
347 pharmacological inhibition of UCH-L1 in neuroinflammation-associated pathology, which could
348 include dementia.

349 **Figure 1**

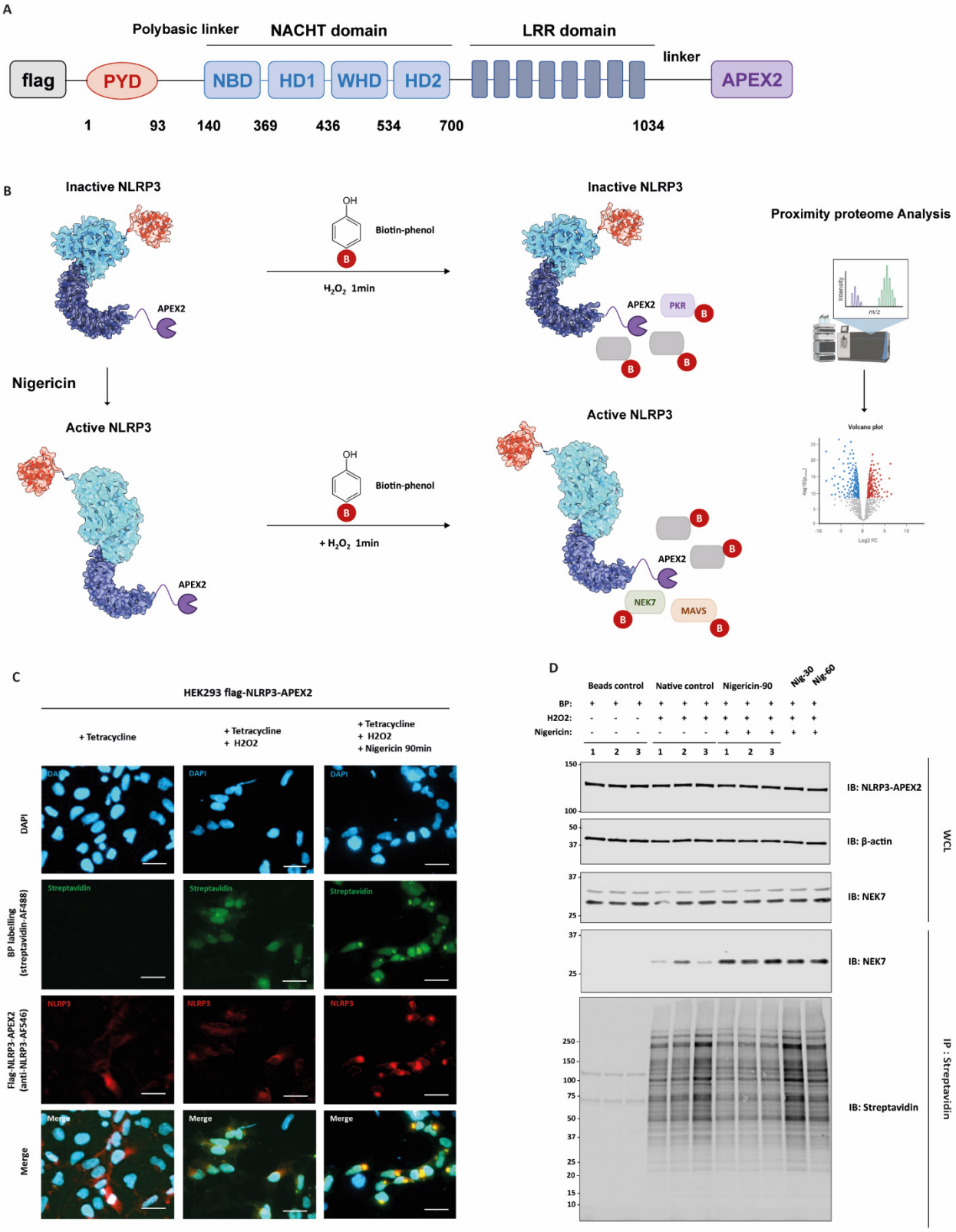

350

351 **Figure 1 | Proximity proteomic profiling of the NLRP3 inflammasome upon activation**

352 (A) Scheme of APEX2-tagging NLRP3. APEX2 was fused to the C terminus of full-length NLRP3 via
353 a glycine-serine linker. (B) Proximity labelling and mass spectrometric analysis workflow for inactive

354 (PDB: 6NPY) and active NLRP3 (PDB: 8EJ4) (Sharif et al., 2019; Xiao et al., 2023). (C) Confocal
355 fluorescence imaging of NLRP3 APEX2 labelling in HEK293 cell lines. NLRP3-APEX2 HEK293
356 stable cell lines were treated with tetracycline overnight, followed by the treatment nigericin (10μM) or
357 DMSO (control) for 90 min. Subsequently, cells were incubated with biotin phenol, followed by H_2O_2
358 as indicated. Afterwards, cells were fixed and stained with streptavidin-Alexa Fluor 488 (AF488)
359 conjugate to visualize biotinylated proteins and anti-NLRP3 antibody to visualize the localization of
360 NLRP3-APEX2. BP, biotinylated proteins. Scale bars, 50 μm. (D) Immunoblot showing the biotinylated
361 NEK7 captured by streptavidin beads in negative control, unstimulated and nigericin-stimulated
362 HEK293 Flp-In T-REx NLRP3-APEX2 cells. Cells were treated with tetracycline overnight, and
363 stimulated with nigericin for 30 min, 60 min, and 90 min before the APEX2 labelling. Whole cell lysates
364 and streptavidin pull-down were collected and blotted for NLRP3 and NEK7.

365

366

367

368

369

370

371

372

373

374

375

376

377

378

379

380

381

Figure 2

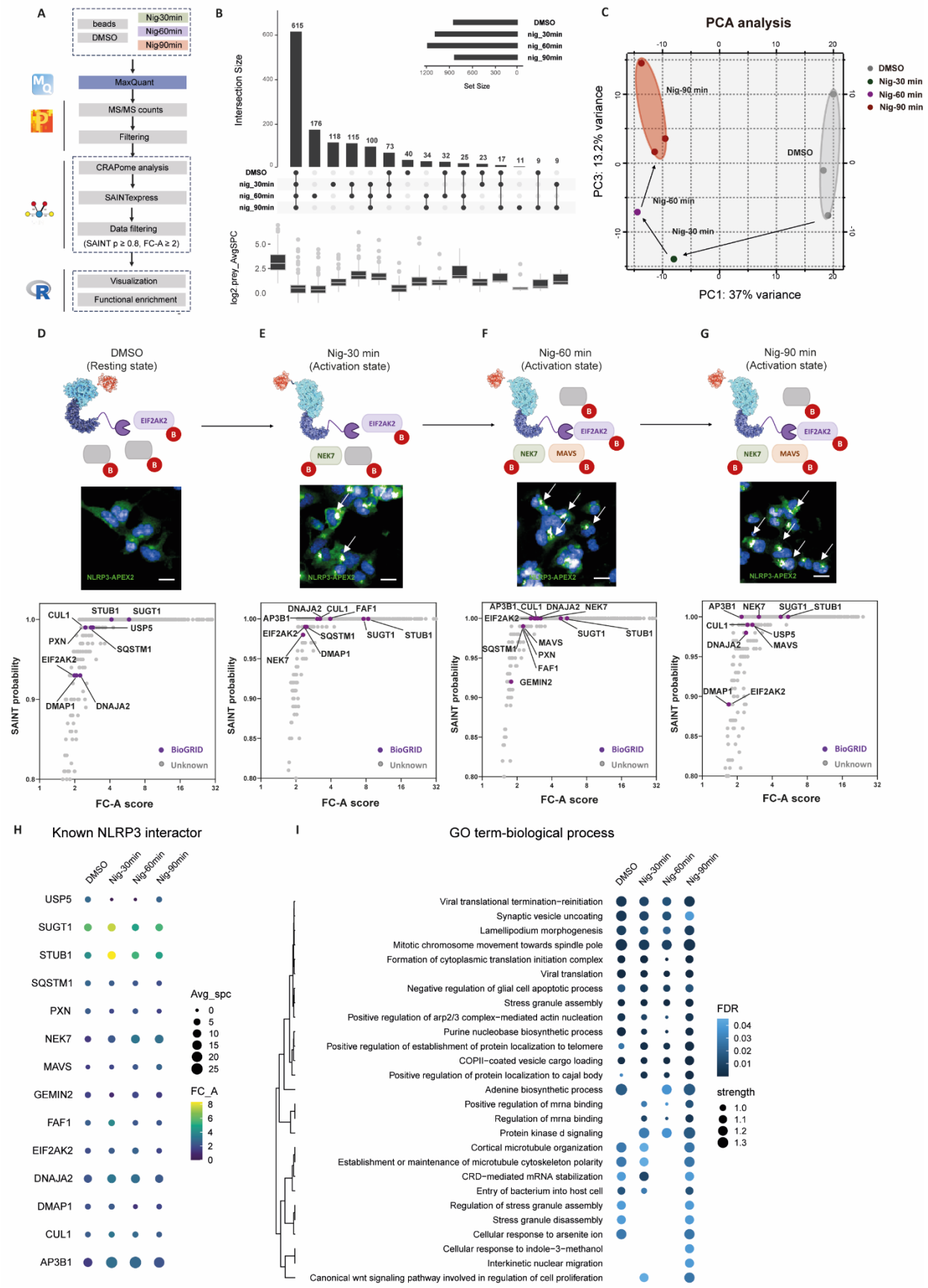
A
beads
DMSO
Nig30min
Nig60min
Nig90min
MaxQuant
MS/MS counts
Filtering
CRAPome analysis
SAINTexpress
Data filtering
(SAINT p ≥ 0.8, FC-A ≥ 2)
Visualization
Functional enrichment
B
Intersection Size
Set Size
log2 prey_AvgSPC
C
PCA analysis
PC3: 13.2% variance
PC1: 37% variance
Nig-90 min
Nig-60 min
Nig-30 min
DMSO
D
DMSO
(Resting state)
E
Nig-30 min
(Activation state)
F
Nig-60 min
(Activation state)
G
Nig-90 min
(Activation state)
EIF2AK2
NEK7
MAVS
NLRP3-APEX2
SAINT probability
FC-A score
BioGRID
Unknown
H
Known NLRP3 interactor
Avg_spc
FC_A
I
GO term-biological process
FDR
strength

Figure 2 | Temporal tracking of the NLRP3 proximity proteome

(A) Schematic illustration of the data analysis for APEX2 PL-MS. (B) The upset plot depicting the intersections of high confidence NLRP3 proximal proteins across samples. The bars in the y axis represent the number of high confidence proximal proteins (SAINT probability score ≥ 0.8, fold change ≥ 2) identified in each sample. The boxplot represents the log2 (average of spectral counts) of the proximal proteins identified in each group. The median, first and third quartiles of the data were displayed as the centre line, the lower and upper boundaries. (C) Principal component analysis of the 8 samples (3 unstimulated DMSO controls, 3 stimulated samples with 90 min treatment of nigericin, 30min nigericin-stimulated samples, and 60 min nigericin-stimulated samples). Each dot represents an individual samples. (D-G) SAINT probability scoring of the proteomic data for NLRP3-APEX2 compared to the negative beads control. Proteins passing the cut off (SAINT probability score ≥ 0.8 and FC-A score ≥ 1) are considered as high confidence proximal proteins for NLRP3. Previously reported NLRP3-interacting proteins (BioGRID, v4.4.213) are coloured in purple. All other proteins are shown in grey. Inactive (PDB: 6NPY) and active NLRP3 (PDB: 8EJ4) are shown as surface view with model. (H) Dot plot of previously reported NLRP3-interacting proteins that are detected in the NLRP3-APEX2 proximitome upon nigericin stimulation for different time points (unstimulated, 30 min, 60 min, and 90 min). Sizes denote the average spectral counts and colours denote the FC-A score. (I) Dot plots displaying the GOBP enrichment analysis of high confidence NLRP3 proximal proteins upon nigericin stimulation for different timepoints as indicated.

419 **Figure 3**

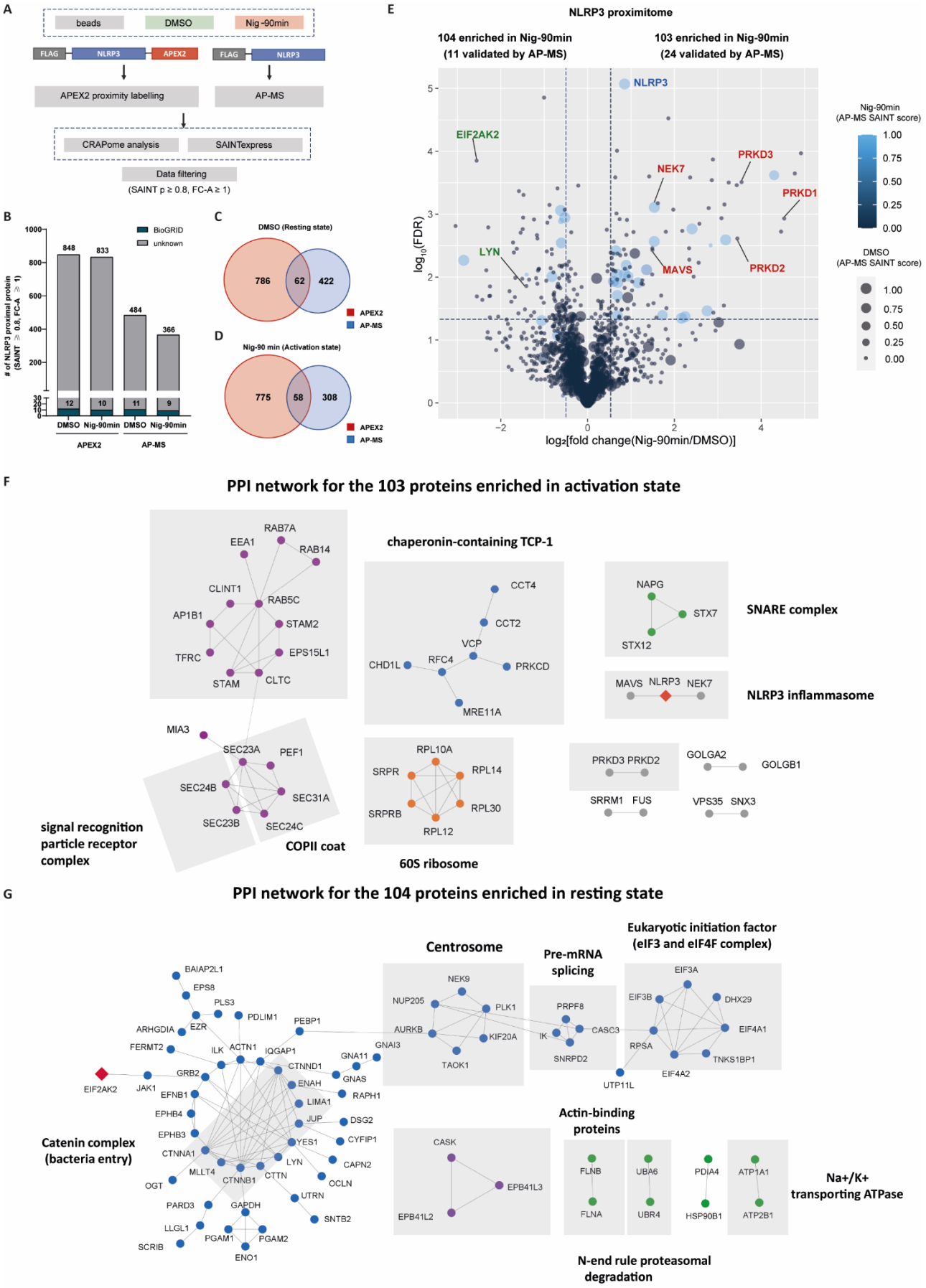

420

Figure 3 | Mapping stimulation-dependent NLRP3 PPI alterations using APEX2-PL and AP-MS

(A) Schematic of the integrated approach combining APEX2 proximity labelling and AP-MS. (B) The number of known (BioGRID, blue) and newly discovered NLRP3-interacting proteins (grey) from APEX2 proximity labelling or AP-MS. (C-D) Venn diagrams showing the number of NLRP3 proximal proteins identified in APEX2 proximity labelling or AP-MS. (E) Volcano plot depicting the fold change for relative protein quantification of NLRP3-APEX2 proximity labelling samples between unstimulated (DMSO) and stimulated conditions (nigericin-90min). Data are shown as means of three independent samples. Non-adjusted unpaired two-tailed t-test was applied to the statistical analysis. Sizes denote the SAINT probability score for AP-MS during stimulation (nigericin-90min), and colours reflect the score in its unstimulated condition. (F-G) Protein-protein interaction network for NLRP3-APEX2 proximity labelled proteins enriched after stimulation with nigericin (F) or unstimulated as control (G). MCL algorithm was performed with the PPI scores from STRING database (confidence score threshold = 0.7). Grey lines denote the high-confidence protein-protein interaction curated from Reactome, CORUM and IntAct database. Cluster labels were added manually. n = 3 biological replicates.

Figure 4

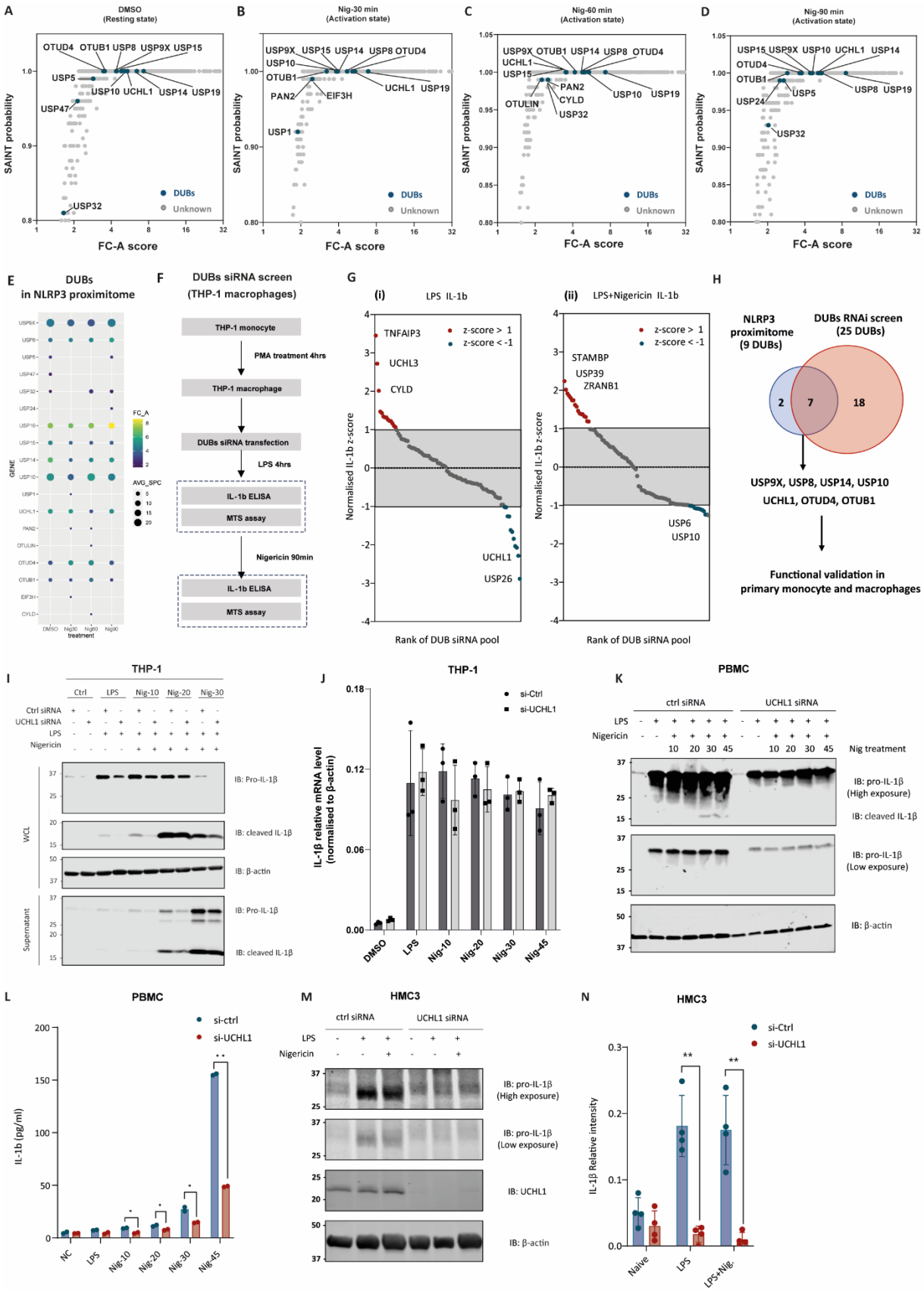
A
DMSO
(Resting state)
OTUD4 OTUB1 USP8 USP9X USP15
USP5
USP10 UCHL1 USP14 USP19
USP47
USP32
SAINT probability
FC-A score
DUBs
Unknown
B
Nig-30 min
(Activation state)
USP9X USP15 USP14 USP8 OTUD4
USP10
OTUB1
PAN2
EIF3H
UCHL1 USP19
USP1
C
Nig-60 min
(Activation state)
USP9X OTUB1 USP14 USP8 OTUD4
UCHL1
USP15
PAN2
CYLD
USP32
OTULIN
USP10 USP19
D
Nig-90 min
(Activation state)
USP15 USP9X USP10 UCHL1 USP14
OTUD4
OTUB1
USP5
USP8 USP19
USP24
USP32
E
DUBs
in NLRP3 proximitome
GENE
FC_A
AVG_SPC
treatment
F
DUBs siRNA screen
(THP-1 macrophages)
THP-1 monocyte
PMA treatment 4hrs
THP-1 macrophage
DUBs siRNA transfection
LPS 4hrs
IL-1b ELISA
MTS assay
Nigericin 90min
IL-1b ELISA
MTS assay
G
(i) LPS IL-1b
TNFAIP3
UCHL3
CYLD
z-score > 1
z-score < -1
UCHL1
USP26
Normalised IL-1b z-score
Rank of DUB siRNA pool
(ii) LPS+Nigericin IL-1b
STAMBP
USP39
ZRANB1
USP6
USP10
H
NLRP3
proximitome
(9 DUBs)
DUBs RNAi screen
(25 DUBs)
2
7
18
USP9X, USP8, USP14, USP10
UCHL1, OTUD4, OTUB1
Functional validation in
primary monocyte and macrophages
I
THP-1
Ctrl
LPS
Nig-10
Nig-20
Nig-30
Ctrl siRNA
UCHL1 siRNA
LPS
Nigericin
WCL
Supernatant
IB: Pro-IL-1β
IB: cleaved IL-1β
IB: β-actin
J
THP-1
si-Ctrl
si-UCHL1
IL-1β relative mRNA level
(normalised to β-actin)
DMSO
LPS
Nig-10
Nig-20
Nig-30
Nig-45
K
PBMC
ctrl siRNA
UCHL1 siRNA
LPS
Nigericin
Nig treatment
IB: pro-IL-1β
(High exposure)
IB: cleaved IL-1β
IB: pro-IL-1β
(Low exposure)
IB: β-actin
L
PBMC
si-ctrl
si-UCHL1
IL-1b (pg/ml)
NC
LPS
Nig-10
Nig-20
Nig-30
Nig-45
M
HMC3
ctrl siRNA
UCHL1 siRNA
LPS
Nigericin
IB: pro-IL-1β
(High exposure)
IB: pro-IL-1β
(Low exposure)
IB: UCHL1
IB: β-actin
N
HMC3
si-Ctrl
si-UCHL1
IL-1β Relative intensity
Naive
LPS
LPS+Nig.

461 **Figure 4 | Proximity proteome-guided RNAi screen identifies deubiquitinases that are involved in**
462 **IL-1β production**

463 (A-D) APEX2 proximity labelling identifies DUBs in the local milieu of NLRP3 upon nigericin
464 stimulation. SAINT probability scoring of the proteomic data for NLRP3-APEX2 compared to the
465 negative beads control. Proteins passing the cut off (SAINT probability score ≥ 0.8 and FC-A score ≥
466 1) are considered as high confidence proximal proteins for NLRP3. Deubiquitinases are coloured in
467 blue and all other proteins are shown in grey. (E) Dot plots showing the DUBs in the NLRP3 proximity
468 proteome upon nigericin stimulation for different time points as indicated. Sizes denote the average
469 spectral counts and colours denote the FC-A score. (F) Schematic of experimental design for the DUB
470 siRNA library screen. (G) z-scores distribution of the IL-1β in the supernatant for individual siRNAs.
471 The RNAi screen is carried out in PMA-differentiated THP-1 cells upon LPS (i) or LPS+NIG treatment
472 (ii), using ELISA for the measurement of IL-1β in the supernatant. Hits with a z-score of ≤ -1 or ≥1 are
473 chosen as candidates for further validation. (H) Venn diagrams showing the intersection between the
474 hits identified through APEX2-PL and siRNA screen. (I-J) Immunoblot and RT-qPCR analysis of
475 whole cell lysates and supernatants from THP-1 cells transfected with non-targeting control siRNA, or
476 UCH-L1-specific siRNA. Cells were differentiated with PMA and primed with LPS (1 μg/mL) for 4
477 hours, followed by the treatment of nigericin (10 μM) for different timepoints as indicated. (K-L)
478 PBMCs were transfected with non-targeting control, or UCH-L1-specific siRNA, stimulated with LPS
479 for 4 hours and nigericin for different timepoints as indicated. (K) Immunoblot of cell lysates from
480 PBMCs. (L) Production of IL-1β in the supernatants from PBMCs as measured by ELISA. *$p < 0.05$,
481 **$p < 0.01$ (unpaired two-sided t-test). The results are representative of 3 independent experiments. (M-
482 N) Immunoblot of cell lysates from HMC3 cells transfected with non-targeting control siRNA or UCH-
483 L1-specific siRNA. Cells were primed with LPS (1 μg/mL) for 4 hours, followed by the treatment of
484 nigericin (10 μM) for 45 minutes. (N) IL-1β bands were quantified using GelAnalyzer and normalised
485 using β -actin bands. Error bars show the standard deviation of the mean. **$p < 0.01$ (unpaired two-
486 sided t-test).

487

488

489

490

491

492

493

494 **Figure 5**

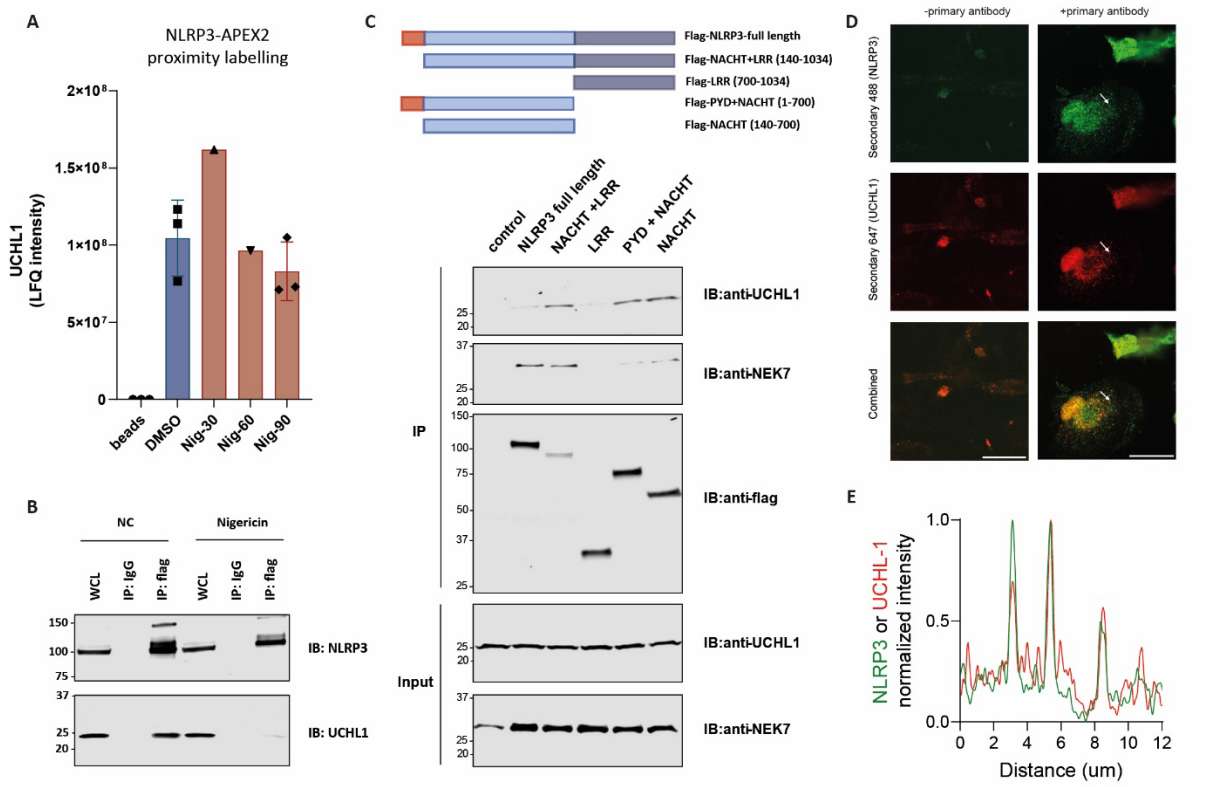

495

496 **Figure 5 | UCH-L1 interacts with the NACHT domain of NLRP3**

497 (A) The raw LFQ Intensity of UCH-L1 protein identified in the APEX2 proximity labelling performed
498 in this study across all the samples including beads Control, DMSO Control and Nigericin treatment at
499 different time points. Experiment was performed in triplicate except of Nig-30 and Nig-60 where only
500 1 replicant was performed. (B) Flp-In T-Rex 293 NLRP3-flag stable cells were induced with
501 tetracycline overnight. Afterwards, cells were treated with DMSO or Nigericin for 90 minutes. NLRP3-
502 flag was pulled down using anti-flag antibody or IgG and immunoblotted with indicated antibodies. (C)
503 Schematic representation of the N-terminal Flag-tagged NLRP3 domain constructs: full length NLRP3,
504 NACHT and LRR domain NLRP3 (Flag-NACHT+LRR, amino acids 140-1034), LRR domain of
505 NLRP3 (Flag-LRR, amino acids 700-1034), pyrin and NACHT domain of NLRP3 (Flag-
506 PYD+NACHT, amino acids 1-700), NACHT domain of NLRP3 (Flag-NACHT, amino acids 140-700).
507 HEK293T cells were transfected with the appropriate NLRP3 plasmid using Lipofectamine 3000. Cells
508 were cultured for 24 hours before they were lysed. NLRP3 domain-flag was pulled down using anti-
509 flag antibody and immunoblotted with indicated antibodies. (D) Fluorescence confocal images of
510 hiPSC-derived microglial cells stained for UCHL-1 and NLPR3. UCHL-1 and NLRP3 show
511 colocalization, but only when cells were stained with primary antibodies for UCHL-1 and NLRP3 (right
512 column). No colocalization is shown when cells are not stained with primary antibodies against UCHL-
513 1 and NLRP3 (left column). (E) Line profile showing the min-max normalized intensity of UCHL-1

514 (red) and NRLP3 (green) along and in the direction of the white arrow indicated in (D). The peaks in
515 normalized intensity indicate colocalization of NLRP3 and UCHL-1 in enriched areas (or 'specks') of
516 NLRP3.
517
518
519
520
521
522
523
524
525
526
527
528
529
530
531
532
533
534
535
536
537
538
539
540

541 **Figure 6**

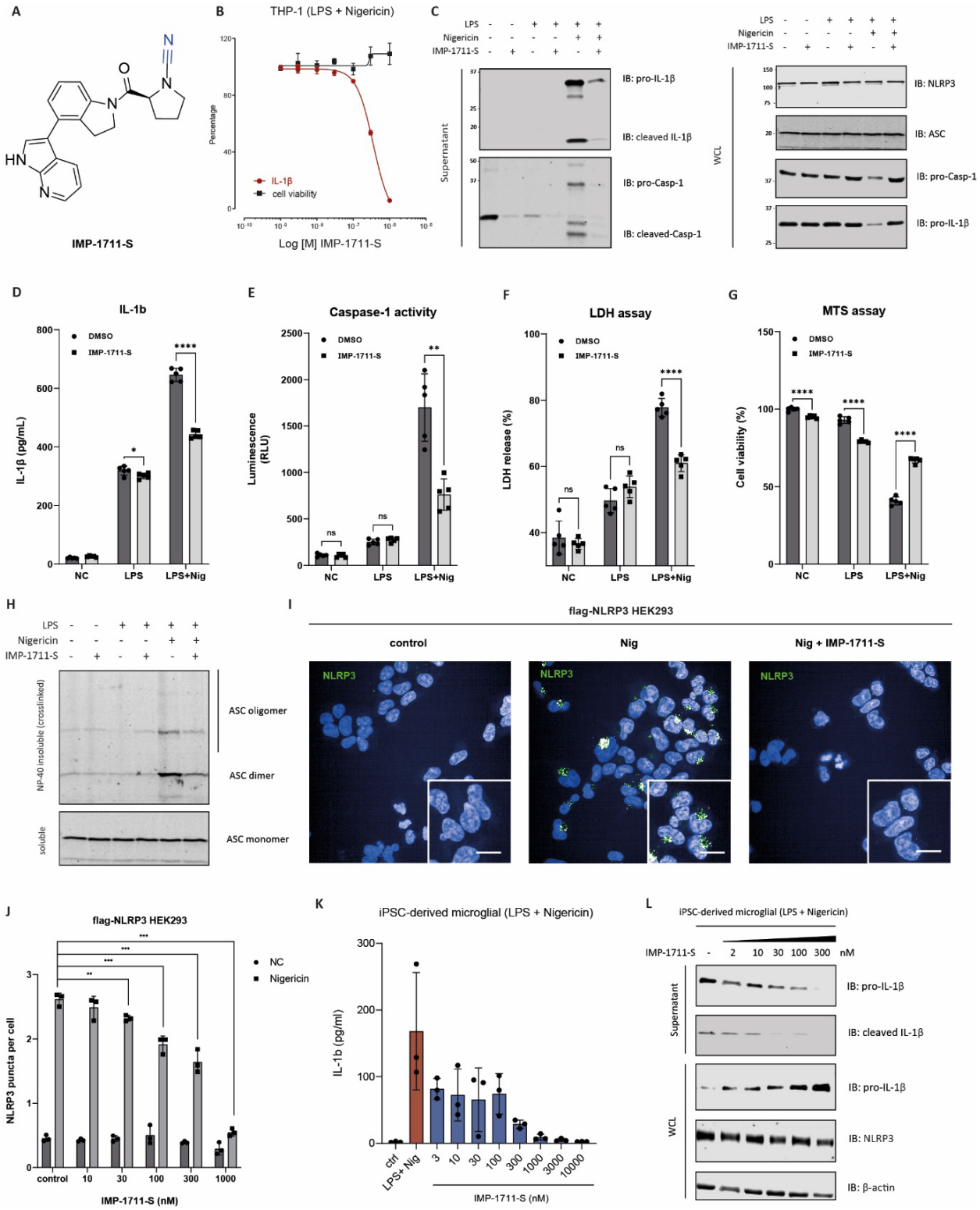

542

543

544

545

546 **Figure 6 | UCH-L1 inhibitor blocks ASC/NLRP3 assembly and IL-1β production**
547 (A) UCH-L1 inhibitor IMP-1711-S structure. (B) Red, production of IL-1β from PMA-differentiated
548 THP-1 cells stimulated with LPS and nigericin and treated with IMP-1711-S (3-10,000 nM) as measure
549 by ELISA (red). Black, cell viability measured by MTS assay. Data are expressed as mean ± s.d., n = 3
550 biologically independent samples. (C-G) THP-1 cells were differentiated with PMA and primed with
551 LPS (1 μg/mL) for 4 hours, followed by the treatment of nigericin (10 μM) for 45 minutes. DMSO or
552 IMP-1711-S (0.3 μM) was added at the same time with LPS. (C) Immunoblot analysis of whole cell
553 lysates and supernatants from THP-1 cells treated with DMSO or IMP-1711-S. (D-E) Supernatants
554 were collected for the measurement of IL-1β (D), Caspase-1 activity (E) from 3 independent
555 experiments. *$p < 0.05$, **$p < 0.01$, ***$p < 0.001$, ****$p < 0.0001$ (unpaired two-sided t-test).
556 Additionally, the cell viability was measured using LDH assay (F) and MTS assay (G). (H) Immunoblot
557 analysis of ASC polymerization upon treatment of DMSO or IMP-1711-S. (I-J) Immunofluorescence
558 imaging of flag-NLRP3 HEK293 stable cells treated with DMSO or IMP-1711-S (300nM), followed
559 by the stimulation with nigericin. Scale bars, 10 μm. (J) Quantitative analysis of the NLRP3 puncta
560 formation upon nigericin treatment in the presence of DMSO or different doses of IMP-1711-S (0.001-
561 1μM) as indicated. **$p < 0.01$, ***$p < 0.001$. (K) IL-1β levels were determined using ELISA from the
562 supernatant of fully differentiated hiPSC-derived microglia. Cells were primed with LPS (1 μg/mL) for
563 4 hours, followed by the treatment of nigericin (10 μM) for 45 minutes. IMP-1711-S inhibitor was
564 added simultaneously with LPS at different concentrations. (L) Immunoblot analysis of whole cell
565 lysates and supernatants from hiPSC-derived microglia treated with DMSO or different concentrations
566 of IMP-1711-S as indicated.

567

568

569

570

571

572

573

574

575

576

577

578 **Figure 7**

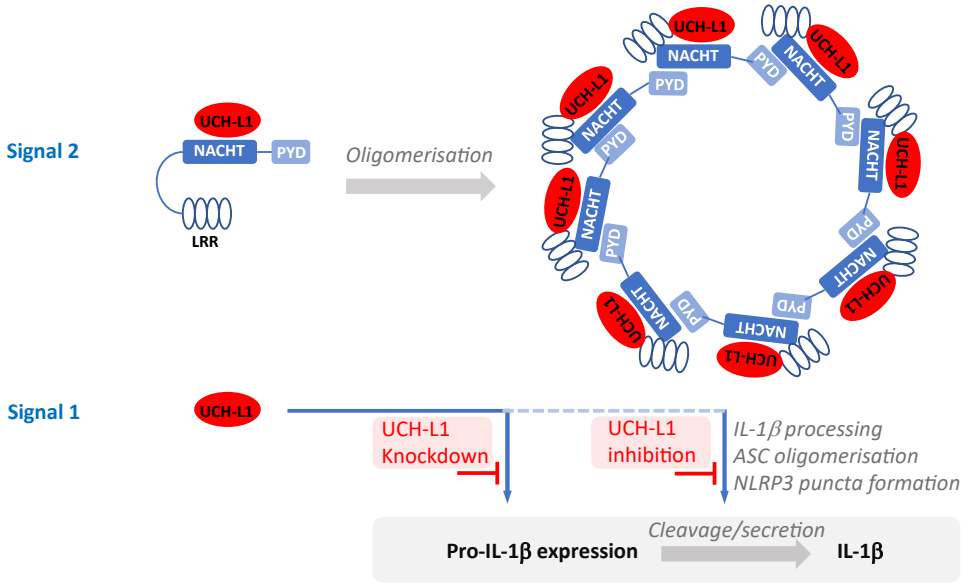

579

580 **Figure 7 | Model illustrating multi-functional roles of UCH-L1 in the NLRP3-mediated IL-1β**
581 **expression, processing and production.** UCH-L1 was shown previously to play a role in NF-κB
582 signalling, affecting pro-IL-1β expression (Zhang et al., 2021) in the context of signal 1. UCH-L1
583 deletion or pharmacological inhibition interferes with IL-1β production through processes of signal 2
584 (nigericin) involving ASC oligomerisation, thereby blocking IL-1β processing and secretion.

585

586

587 **STAR★Methods**

588 **Key resources table**

REAGENTS or RESOURCE	SOURCE	IDENTIFIER
Antibodies		
Cleaved IL-1 β (Asp116)	Cell Signalling Technology	CAT# 83186
IL-1β	Cell Signalling Technology	CAT# 12703
Caspase-1	Cell Signalling Technology	CAT# 2225
NLRP3	Cell Signalling Technology	CAT# 15101
ASC(B-3)	Santa Cruz	CAT# sc-514414
β-Actin	Sigma-Aldrich	CAT# A5441
NEK7	Abcam	CAT# ab133514
UCHL1	Santa Cruz	CAT# sc-271639
IRDye® 800CW Goat anti-Rabbit IgG Secondary Antibody	LI-COR	CAT# 926-32211
IRDye® 800CW Goat anti-Mouse IgG Secondary Antibody	LI-COR	CAT# 926-32210
IRDye® 680RD Goat anti-Mouse IgG Secondary Antibody	LI-COR	CAT# 926-68070
IRDye® 680RD Goat anti-Rabbit IgG Secondary Antibody	LI-COR	CAT# 926-68071
Goat anti-Rabbit IgG (H+L) secondary, Alexa Fluor 488-conjugated	Invitrogen	CAT# A-11008
Goat anti-Mouse IgG (H+L) secondary, Alexa Fluor 488-conjugated	Invitrogen	CAT# A-11001
Cell lines and tissue culture reagents		
THP-1	ATCC	TIB-202
HEK293T	ATCC	CRL-3216
Human PBMC	Clinical partners	N/A
KOLF2.1S hiPSC	HipSci project	N/A
Flp-In T-REx 293 Cell Line	Invitrogen	R78007
L-Glutamine (200 mM)	Gibco	25030149
Fetal Bovine Serum	Gibco	10100147
Poly-D-Lysine	Gibco	A3890401
GlutaMAX Supplement	Gibco	35050061
β-Mercaptoethanol	Sigma-Aldrich	M6250
RPMI-1640 Medium	Sigma-Aldrich	R0883

PMA/Phorbol 12-myristate 13-acetate	Sigma-Aldrich	P1585
Penicillin-Streptomycin (10,000 U/mL)	Gibco	15140122
Zeocin	InvivoGen	ant-zn-1
blasticidin	InvivoGen	ant-bl-1
hygromycin B	InvivoGen	ant-hg-1
Puromycin Dihydrochloride	Thermo Scientific	A1113803
Dimethyl sulfoxide	Sigma-Aldrich	D8418
Dulbecco's Phosphate Buffered Saline	Sigma-Aldrich	D8537
Chemicals, peptides, and recombinant proteins		
Suberic acid bis(N-hydroxysuccinimide ester)	Sigma-Aldrich	S1885
Sodium deoxycholate	Sigma-Aldrich	D6750
Ultrapure LPS, E. coli 0111:B4	InvivoGen	tlrl-3pelps
Cycloheximide solution	Sigma-Aldrich	C4859-1ML
Bafilomycin A1 from Streptomyces griseus	InvivoGen	B1793
16% Formaldehyde (w/v), Methanol-free	Thermo Scientific	28906
PhosSTOP phosphatase inhibitor	Roche	4906837001
cOmplete™, Mini, EDTA-free Protease Inhibitor Cocktail	Roche	11836170001
Trichloroacetic acid	Sigma-Aldrich	T6399
Pierce™ DTT (Dithiothreitol)	Thermo Scientific	20290
Iodoacetamide	Sigma-Aldrich	A3221
Lipofectamine™ 3000 Transfection Reagent	Invitrogen	L3000001
Lipofectamine™ 2000 Transfection Reagent	Invitrogen	11668030
Lipofectamine™ RNAiMAX Transfection Reagent	Invitrogen	13778100
Sequencing-grade modified trypsin	Promega	V5111
Tween-20	Sigma-Aldrich	P1379-1L
Triton X-100	Sigma-Aldrich	T9284-500ML
Bromophenol blue	Sigma-Aldrich	B0126
Biotin	Sigma-Aldrich	B4501
PMSF	G-Biosciences	786-055
Hydrogen peroxide (H_2O_2), 30% (wt/wt)	Sigma-Aldrich	H1009-100ML
Trifluoroacetic acid	Sigma-Aldrich	91707
Formic acid	Sigma-Aldrich	56302

Biotin-phenol		
Dynabeads™ MyOne™ Streptavidin T1	Invitrogen	65602
Sodium ascorbate	Sigma-Aldrich	A7631
Trolox	Sigma-Aldrich	238813-5G
Sodium azide	Sigma-Aldrich	S2002
MG132, Ready Made Solution	Sigma-Aldrich	M7449-1ML
TCEP	Gold Biotechnology	TCEP2
IGEPAL® CA-630	Sigma-Aldrich	I8896
Triton™ X-100	Sigma-Aldrich	X100
Nuclease-Free Water (not DEPC-Treated)	Invitrogen	AM9932
Benzonase® Nuclease	Millipore	E1014
Biochemistry assays		
Caspase-Glo® 1 Inflammasome Assay	Promega	G9951
Pierce™ BCA Protein Assay Kit	Thermo Scientific	23225
InstantBlue® Coomassie Protein Stain (ISB1L)	Abcam	ab119211
CyQUANT™ LDH Cytotoxicity Assay	Invitrogen	C20300
CellTiter 96® AQueous One Solution Cell Proliferation Assay (MTS)	Promega	G3582
Dynabeads™ Co-Immunoprecipitation Kit	Invitrogen	14321D
Human IL-1 beta/IL-1F2 DuoSet ELISA	R&D Systems	DY201
Human IL-6 DuoSet ELISA	R&D Systems	DY206
Human TNF-alpha DuoSet ELISA	R&D Systems	DY210
LightCycler® 480 SYBR Green I Master	Roche	04707516001
High-Capacity cDNA Reverse Transcription Kit	Thermo Scientific	4368814
RNeasy Mini Kit	Qiagen	74104
Stop Solution 2N Sulfuric Acid	R&D Systems	DY994
Recombinant DNA		
pOG44 Plasmid Vector	ThermoFisher Scientific	CAT# V600520
pcDNA5/FRT/TO GFP	Addgene	CAT# 19444
pcDNA5/FRT/TO APEX2-NLRP3-Flag	Generated in this study (Backbone 19444)	N/A
pEGFP-C2-NLRP3 (ITEM 73955)	Addgene	N/A
pNLRP3 FLAG Full length	Generated in this study (Backbone 73955)	N/A

pNLRP3 NACHT+ LRR- FLAG (140-1035)	Generated in this study (Backbone 73955)	N/A
pNLRP3 LRR only- FLAG (700-1035)	Generated in this study (Backbone 73955)	N/A
pNLRP3 Pyrin + NACHT- FLAG (1-700)	Generated in this study (Backbone 73955)	N/A
pNLRP3 NACHT only- FLAG (140 -700)	Generated in this study (Backbone 73955)	N/A
Software and algorithms		
Prism	GraphPad, version 9	https://www.graphpad.com/scientific-software/prism/
Perseus	Nature methods 13.9 (2016): 731-740. Version 1.6.15.0	https://maxquant.net/perseus/
ImageStudioLite	LI-COR, version 5.2	https://www.licor.com/bio/image-studio-lite/
FiJi	Nature Methods, 9(7), 676–682.	https://imagej.net/software/fiji/
Cytoscape	Genome Research 2003 Nov; 13(11):2498-504	https://cytoscape.org/
ZEN	Carl Zeiss	RRID: SCR_013672
Illustrator	Adobe	https://www.adobe.com/uk/
Photoshop	Adobe	https://www.adobe.com/uk/
MaxQuant	Nat Protoc. 2016 Dec;11(12):2301-2319. Version v1.6.10.43	http://www.maxquant.org

589

590 **Method details**

591 **Cell culture**

592 THP-1 cells were cultured in 10% FBS (Gibco #10500-64) RPMI 1640 (Sigma) supplemented with 2%
593 L-glutamine (G7513, Sigma-Aldrich), 0.05 mM β-mercaptoethanol (Sigma), and antibiotics
594 (penicillin/streptomycin, Gibco). HEK293T cells were cultured in high glucose DMEM, supplemented
595 with 10% FBS, and 2% L-glutamine. Flp-In T-REx 293 cell line (R78007, ThermoFisher) were cultured
596 in high glucose DMEM, supplemented with 10% FBS, 2% L-glutamine, 100 µg/mL Zeocin (InvivoGen,
597 ant-zn-1) and 15 µg/mL blasticidin (InvivoGen, ant-bl-1) at 37 °C in a humidified 5% CO2 atmosphere.
598 The stably transfected Flp-In T-REx 293 cell lines (flag-NLRP3 and flag-NLRP3-APEX2) were
599 cultured in the same medium and selected by 100 µg/mL hygromycin B (InvivoGen, ant-hg-1). 1 µg/mL
600 tetracycline was added to induce the expression of flag-NLRP3 or flag-NLRP3-APEX2.

601 **PBMC isolation and *in vitro* culture**

602 To isolate the mononuclear cells, leukocyte cones (around 4 mL) were diluted in 25 mL RPMI medium
603 before laid onto 15 mL LymphoPrep without disturbing the interface between LymphoPrep and the
604 cone blood. Subsequently, it was centrifuged at 2000 rpm (400 g) at room temperature for 20 min.

605 Lymphocytes, which form a thin layer of white film after the centrifuge, are transferred into a fresh 50
606 mL tube with a Graduated Pasteur Pipette and washed twice with RPMI medium. PBMCs were plated
607 in 6-well plate at 1-2 × 10^7 cells/mL in 10 mL and allowed to adhere at 37°C for 4 hrs. Non-adherent
608 cells were removed thorough washing with RPMI-1640.

609 **hiPSC culture and differentiation to microglia**

610 The KOLF2.1S hiPSC line used for this study was obtained with informed consent from all subjects,
611 donors and/or their legal guardian(s) and with the approval of all the relevant institutions. All methods
612 and experimental protocols were carried out in accordance with University of Oxford guidelines and
613 regulations. hiPSC lines were generated previously as part of the HipSci project (REC Reference
614 09/H0304/77, covered under HMDMC 14/013 and REC reference 14/LO/0345). KOLF2.1S was
615 generated from the parental KOLF2-C1 line (https://hpscreg.eu/cell-line/WTSIi018-B-1) itself a clonal
616 isolate of KOLF2 (https://hpscreg.eu/cell-line/WTSIi018-B) by correction of a heterozygous loss of
617 function mutation ARID2 using CRISPR based homology repair by the Cellular Operations Gene
618 Editing team at the Wellcome Sanger Institute (Bruntraeger et al., 2019). hiPSC were cultured in OxE8
619 medium with daily media changes (Vaughan-Jackson et al., 2021) on Geltrex (Gibco A1413302) coated
620 tissue culture dishes and passaged with 0.5mM EDTA. hiPSC were differentiated into microglial
621 precursors through the formation of embryoid bodies (EB) (van Wilgenburg et al., 2013) by seeding 4
622 x 10^6 hiPSC per well of an Aggrewell 800 plate (STEMCELL Technologies, 34815) in EB medium
623 (OxE8 supplemented with 50 ng/mL BMP4 (PeproTech PHC9534), 50 ng/mL VEGF (PeproTech
624 PHC9394), and 20 ng/mL SCF (Miltenyi Biotec 130-096-695)). After differentiating in EB media for
625 6 days (with daily 50% media changes), 150 EB were transferred to T175 coated with 0.1% Gelatin
626 containing differentiation media (X-VIVO 15 (Lonza BE02-060F), 1x GlutaMAX (Lifetech 25050-
627 061), 50µM β-mercaptoethanol (LifeTech 31350-010), 100 ng/mL M-CSF (Gibco, PHC9501), 25
628 ng/mL IL-3 (Gibco, PHC0033). After 4-5 weeks of differentiation, microglial precursors shed into the
629 media are harvested weekly by collection of supernatant and pelleting at 400 x g for 5 minutes.
630 Microglial precursors are then resuspended in the final microglia maturation media ITMG
631 (ADMEM/F12 (LifeTech, 12634-010), 1x GlutaMAX (Lifetech, 25050-061), 100 ng/mL IL-34
632 (PeproTech, 200-34-500), 50 ng/mL TGFβ-1 (PeproTech, 100-21C-250), 25 ng/mL M-CSF (Gibco,
633 PHC0033), 10 ng/mL GM-CSF (Gibco, PHC2013), as previously described (Washer et al., 2022), and
634 differentiated to hiPSC-microglia for 14 days, with 50% media changes every 3 to 4 days. All
635 differentiation steps are carried out at 37°C, 5% CO2.

636 **Inflammasome activation assay**

637 THP-1 cells were plated in a concentration of 1x10^6 cells/mL and incubated with 0.5 µM PMA for 4 h.
638 After differentiation, PMA-containing media was replaced with fresh media. Experiments were carried
639 out on the following day. Differentiated THP-1 cells were primed with LPS (1 µg/mL) for 4 h, followed

640 by the treatment of PBS (mock) or 5 μM nigericin for 45 min. After stimulation, supernatants and cell
641 lysates were collected separately, or combined together for immunoblotting analysis.

642 **ASC speck oligomer crosslinking**

643 PMA-differentiated THP-1 cells were primed with LPS (1 μg/mL) for 4 h, and then stimulated with
644 nigericin (10μM) for 45 min. Cells were lysed on ice in Buffer A (20 mM HEPES-KOH, pH 7.5, 10
645 mM KCl, 1.5 mM $MgCl_2$, 1 mM EDTA, 1 mM EGTA, 320 mM sucrose, and protease inhibitor cocktail),
646 and homogenized using a 21-gauge needle. The lysates were centrifuged at 1,800 rpm (300 g) for 8 min
647 at 4 °C. Supernatants were transferred to a new tube and diluted with 1 volume of CHAPS buffer (20
648 mM HEPES-KOH, pH 7.5, 5 mM MgCl2, 0.5 mM EGTA, 0.1% CHAPS, and protease inhibitor
649 cocktail). The diluted lysates were then centrifuged at 5,000 rpm (2,400 g) provide g for 8 min to obtain
650 the crude inflammasome-containing pellets. The pellets were washed with ice cold PBS twice,
651 resuspended in CHAPS buffer, and then cross-linked at 37 °C for 20 min by adding 2mM DSS
652 (disuccinimidyl suberate, dissolved in DMSO). The reaction was quenched by adding SDS sample
653 buffer and followed by Western blotting analysis.

654 **Enzyme-linked immunosorbent assay (ELISA)**

655 Human IL-1β (DY201, R&D Systems) and IL-6 (DY206, R&D Systems) production in the supernatants
656 were detected by ELISA kit according to manufacturer's protocol. Plates were coated with diluted
657 capture antibody in sterile PBS at room temperature overnight. On the following day, plates were
658 washed three times with 200 μL/well wash buffer (0.05% Tween 20 in PBS, pH 7.2-7.4) before being
659 blocked with 200 μL/well reagent diluent (1% BSA in PBS, pH 7.2-7.4, 0.2 μm filtered) at room
660 temperature for a minimum of 1 h. After blocking, plates were washed three times and incubated with
661 samples or standards (in reagent diluent) for 2 h at room temperature. After three washes of plates, 100
662 μL/well detection antibody (diluted in reagent diluent) was added to the wells and incubated for 2 h at
663 room temperature. Plates were then washed three times and incubated with 100 μL/well Streptavidin-
664 HRP for 20 min at room temperature, followed by another three washes and incubation with 100
665 μL/well substrate solution (1:1 mixture of Colour Reagent A (H_2O_2) and Colour Reagent B
666 (Tetramethylbenzidine)) at room temperature. 20 min after the reaction, 50 μL/well stop solution (2 N
667 H2SO4, DY994, R&D Systems) was added and mixed thoroughly to quench the reaction. The optical
668 density of each well was determined at the wavelength of 450nm, and the relative concentration was
669 calculated based on the standard curve, generated through a 3 parameter logistic curve fit using the data
670 from standard samples.

671 **TCA/DOC protein precipitation**

672 Trichloroacetic acid (TCA)- deoxycholate (DOC) precipitation was commonly used to concentrate the
673 proteins in supernatants and this method was adapted from André et al. Briefly, 8.5 μL of 2% Na-

674 deoxycholate was added to 1 mL sample with a final concentration of 125 μg/mL. This mixture was
675 incubated at room temperature for 15 min and 333 μL of 24% TCA (final concentration 6%) was added
676 to the samples. Proteins were precipitated and centrifuged at 12,000 g for 30 min at 4°C. Supernatant
677 was carefully removed and the pellets were washed once with acetone to remove excessive TCA before
678 another centrifuge at 12,000 g for 5 min. After removing the supernatants, the resulting pellets were
679 solubilised in loading buffer and subjected to immunoblotting analysis.

680 **Cytotoxicity and cell viability assay**

681 Relevant cells were treated as indicated, and the cytotoxicity was detected using CyQUANT™ LDH
682 Cytotoxicity Assay (Invitrogen) according to manufacturer's instruction. Briefly, 50 μL of each sample
683 supernatant was transferred to 96-well flat-bottom plate in triplicate wells, and then, 50 μL of premixed
684 reaction buffer was added to each well. The plate was incubated for 30 min at room temperature before
685 addition of 50 μL/well stop solution. The optical density of each well was measured at the wavelength
686 of 490nm and 680nm (680 nm absorbance was used as background), and the cytotoxicity (% LDH
687 release) was calculated according to manufacturer's protocol.

688 Cell viability was measured using CellTiter 96 AQueous One Solution Cell Proliferation Assay (MTS,
689 Promega). Briefly, 20μl of CellTiter 96® AQueous One Solution Reagent was added to each well
690 containing samples in 100 μl of culture medium. The plate was then incubated for a minimum of 1h at
691 37°C. The absorbance of each well was measured at the wavelength of 490nm, and the cell viability
692 was calculated according to manufacturer's protocol.

693 **Caspase-1 activity bioluminescent assay**

694 Relevant cells were treated as indicated, and the caspase-1 activity in the culture medium (supernatant)
695 was measured using Caspase-Glo® 1 Inflammasome Assay (Promega) according to manufacturer's
696 instruction. Briefly, Caspase-Glo 1 Reagent was prepared through resuspension of Z-WEHD substrate
697 using Caspase-Glo 1 buffer, and the addition of MG132 inhibitor to a final concentration of 60 μM.
698 Afterwards, 50 μL of cell culture medium was transferred to the 96-well plate, followed by adding 5
699 μL Caspase-Glo 1 Reagent. The contents of the wells were thoroughly mixed and incubated at room
700 temperature for at least 1 hour for the signal to be stable. Subsequently, the luminescence value was
701 measured using multi-mode microplate reader FLUOstar Omega (BMG LABTECH) according to
702 manufacturer's instruction.

703 **Immunoprecipitation**

704 Cells were washed with ice-cold PBS for two times, and then lysed in Pierce® IP lysis buffer (25 mM
705 Tris-HCl pH 7.4, 150 mM NaCl, 1% NP-40, 1 mM EDTA, 5% glycerol, PhosSTOP phosphatase
706 inhibitor and cOmplete™ Protease Inhibitor Cocktail). Lysates were incubated on ice for 10 min with
707 periodic mixing, and then clarified at 13,000 g for 10 min at 4°C to remove the cell debris. Pre-cleared

708 lysates were incubated with anti-FLAG® M2 Magnetic Beads at room temperature for 30 min. After
709 three times of washes with TBS, the proteins bound by the anti-flag antibody were pulled down and 3X
710 FLAG® peptide was added for elution. Both the whole cell lysates and the pull-down samples are
711 subjected to immunoblotting analysis.

712 **Transient transfection**

713 For DNA plasmids: Cells were grown in 6-well plates and Lipofectamine 3000 Transfection Reagent
714 (L3000001, ThermoFisher UK) was used to transfect the cells following the manufacturer's instructions.
715 The concentration of plasmids used was indicated in each experiment. For siRNA transfection
716 experiments: Cells were grown in 6-well plates and RNAimax transfection reagent (Invitrogen, 13778-
717 150) was used following the manufacturer's protocol. A final concentration of 10 nM of the following
718 Silencer™ select siRNAs were used: control siRNA (4390844), si-NLRP3 (s41554) and si-UCH-L1
719 (s14616).

720 **Construction of plasmids**

721 The full list and descriptions of all primers and plasmids used in this study can be found in key resources
722 table. For the generation of NLRP3-APEX2, NLRP3-Flag, NEBuilder HiFi DNA Assembly (NEB:
723 E5520S) was used following manufacture protocol. Primers were designed using the NEBuilder
724 Assembly Tool. The successful clones were confirmed using both PCR and DNA sequencing. Finally,
725 the expression plasmids for NLRP3 domains were generated using the Q5® Site-Directed Mutagenesis
726 Kit (NEB: E0554S) following manufacture protocols. We used as a template the GFP- NLRP3 plasmid
727 (Addgene), we initially replace GFP with Flag. Finally, different domains were deleted to generate the
728 successful plasmids. The successful clones were confirmed using both PCR and DNA sequencing.

729 **Generation of stable cell line**

730 The Flp-In T-Rex 293 stable cell lines (flag-NLRP3 and flag-NLRP3-APEX2) were generated using
731 Lipofectamine 3000 following manufacture protocol in a 6-well plate. The cells were transfected with
732 both the expression plasmid and the plasmid pOG44 in a ratio of 1:9. Cells were split the following day
733 and transferred in a 100mm dish. After 8 hours, 300 µg/mL hygromycin B was added into the medium
734 for selection.

735 **sgRNA design, lentivirus production and transduction**

736 Non-targeting control (NTC) and UCH-L1-targeting sgRNA sequences were designed using CRISPick
737 tool (https://portals.broadinstitute.org/gppx/crispick/public). To clone the target sequences into the
738 lentiCRISPRv2 backbone (one vector system), two oligos containing the target sequences were
739 synthesized (Sigma) and inserted into the digested lentiviral construct. sgRNA sequences are as
740 followed: UCH-L1-sgRNA#1: 5'-ACTTCATGAAGCAGACCATT-3'; UCH-L1-sgRNA#2: 5'-

741 AATCGGACTTATTCACGCAG-3'; UCH-L1-sgRNA#3: 5'- AAGACAAACTGGGATTTGGT-3'.
742 HEK293T cell lines were seeded at 40% confluency and transfected with pMD2G, psPAX2 and the
743 above lentiCRISPRv2 plasmids using lipofectamine 2000 following manufacturer's instructions. After
744 incubation for two days, supernatants were collected and filtered by 0.45μm filter, followed by
745 ultracentrifuge to obtain concentrated viral particles.

746 **Biotin-phenol proximity labelling and biotinylated proteins capture**

747 This method was adapted from that previously reported by Stephanie et al. 5×10^6 Flp-In T-Rex HEK293
748 stable cells were induced with 1 μg/mL tetracycline overnight. The next day cells were incubated with
749 medium containing 500 μM biotin-phenol (BP) for 30 min at 37 °C under 5% CO2. Afterwards, a final
750 concentration of 1 mM H_2O_2 was added and incubated for 40 seconds. The reaction was then quenched
751 by the addition of quenching buffer (10mM sodium ascorbate, 10mM sodium azide, 5mM Trolox in
752 DPBS). Subsequently, cells were washed with quenching buffer for three times, PBS for two times and
753 then lysed with RIPA lysis buffer containing 1 mM PMSF, 5 mM Trolox, 10 mM sodium azide, 10 mM
754 sodium ascorbate, PhosSTOP phosphatase inhibitor and cOmplete™ Protease Inhibitor Cocktail.
755 Samples were then briefly sonicated and centrifuged at 10,000 g for 10 min at 4°C to remove cell debris.
756 For streptavidin pull-down experiments, Dynabeads MyOne Streptavidin T1 was prepared and washed
757 with RIPA lysis buffer twice. The cleared lysate was applied to the magnetic beads and at RT for 1 hour.
758 Afterwards, the beads were washed for two times with RIPA lysis buffer, once with 1M KCL, 0.1 M
759 Na_2CO_3 and 2 M Urea (in 10 mM Tris-HCL, pH 8) and finally twice with RIPA buffer again. For
760 western blot analysis, biotinylated proteins were eluted using 60 μL of 3×loading buffer supplemented
761 with 2 mM biotin and 20 mM DTT by boiling (98°C) for 10 min. For Mass spectrometry analysis, an
762 on-beads digestion protocol was used as described below. Samples were denatured in 8 M Urea (in 100
763 mM triethylammonium bicarbonate buffer (TEAB)) and incubated at room temperature for 30 min.
764 Afterwards, the samples were reduced with 10mM tris(2-carboxyethyl)phosphine (TCEP) for at room
765 temperature 30 min. Samples were alkylated by the addition of iodoacetamide (final concentration 50
766 mM) and incubated at room temperature for 30 min. The reaction was quenched by adding DTT (final
767 concentration 20 mM), and the urea concentration were diluted down to 1.5 M by adding TEAB.
768 Biotinylated proteins were digested through the incubation with trypsin (1 μg trypsin per 20 μL
769 streptavidin beads) overnight at 37 °C. Following the trypsinization, samples were desalted using the
770 C18 solid phase cartridge (Sep-Pak, Waters) according to the manufacturer's protocol. Purified peptide
771 eluates were dried down in the speed-vac, re-suspended in buffer A (98 % MilliQ-H20, 2 % CH_3CN
772 and 0.1 % trifluoroacetic acid - TFA) and stored at -20 °C until further analysis.

773 **Affinity-purification mass spectrometry (AP-MS)**

774 1×10^7 HEK293 FLAG-NLRP3 Flp-In T-Rex stable cells were induced with 1 μg/mL tetracycline
775 overnight. The next day cells were incubated with medium with Nigericin (10μM) or DMSO for 90 min

776 at 37 °C under 5% CO_2. Cells were washed with ice-cold PBS for five times, and then lysed in Pierce
777 IP lysis buffer (25 mM Tris-HCl pH 7.4, 150 mM NaCl, 1% NP-40, 1 mM EDTA, 5% glycerol,
778 PhosSTOP phosphatase inhibitor and cOmplete™ Protease Inhibitor Cocktail). Lysates were incubated
779 on ice for 10 min with periodic mixing, and then clarified at 13,000 g for 10 min at 4°C to remove the
780 cell debris. Pre-cleared lysates were incubated with anti-FLAG M2 Magnetic Beads at 4ºC overnight.
781 The next day beads were washed 3 times with TBS. Samples were eluted were eluted using 100 µL of
782 3×loading buffer supplemented 20 mM DTT by boiling (98°C) for 10 min.
783

784 **Mass spectrometry analysis**

785 An Orbitrap Fusion Lumos Tribid mass spectrometer (Thermo Fisher Scientific) coupled to an Ultimate
786 3000 UHPLC (Thermo Fischer Scientific) platform was used to analyse the purified tryptic peptides by
787 liquid chromatography tandem mass spectrometry (LC-MS/MS) as described previously (Davis et al.,
788 2017). In brief, ten per cent of tryptic peptides (~ 200 ng) were loaded onto a trap column (PepMapC18;
789 300µm x 5mm, 5µm particle size, Thermo Fischer) and separated on a 50 cm EasySpray column
790 (ES803, Thermo Fischer) using a 60 minute linear gradient ranging from 2 % to 35% buffer B (A: 5%
791 DMSO, 0.1% formic acid; B: 5% DMSO, 0.1% formic acid in acetonitrile) at a flow rate of ~250
792 nL/min. Eluted peptides were then subjected to electrospray ionisation (ESI) and directed into an
793 Orbitrap Fusion Lumos Tribrid mass spectrometer (instrument control software v3.3). Data were
794 acquired in data-dependent mode (DDA), with the advance peak detection (APD) feature enabled.
795 Survey scans were acquired in the Orbitrap at 120 k resolution over a m/z range 400 -1500, AGC target
796 of 4e5 and S-lens RF of 30. Fragment ion spectra (MS/MS) were obtained in the Ion trap (rapid scan
797 mode) with a Quad isolation window of 1.6, 40% AGC target and a maximum injection time of 35 ms,
798 with HCD activation and 28% collision energy. Raw MS files were analysed using MaxQuant software
799 (v1.6.10.43) using label free quantitation (LFQ) as described previously (Olie et al., 2023). In brief, raw
800 MS files were searched against the UniProtKB human sequence database (UP000005640, 79,038
801 human sequence entries). The following parameters were set to perform label free quantification:
802 Modifications were set on Carbamidomethyl (C) as fixed and Oxidation (M) and Deamidation (NQ) as
803 variable and a maximum of two missed cleavages were allowed. Match between runs function was
804 used.

805 **RNA extraction and real time reverse transcription (RT)-PCR**

806 Total RNA was isolated with the TRIzol reagent (SigmaAldrich) according to the manufacturer's
807 instructions. The nucleic acid concentration was measured with the NanoDrop2000 (NanoDrop
808 Technologies, Inc.). Complementary DNA (cDNA) was synthesized from 1.5 µg of total RNA with the
809 High-Capacity cDNA Reverse Transcription Kit (Applied Biosystems, USA). Quantitative real-time
810 polymerase chain reaction (RT-qPCR) was performed using the LightCycler 480 SYBR Green I Master

811 kit and LightCycler 480 PCR System (Roche, Switzerland) according to the manufacturer's instructions.
812 The Delta-Ct method was used to calculate the relative RNA expression levels.
813

814 **Pathway enrichment analysis**

815 Filtered proximity proteomes (SAINT probability > 0.8, FC-A ≥ 1) either in DMSO control or nigericin
816 activated samples were imported into the STRING database search portal (version 11.5, Szklarczyk et
817 al., 2021; von Mering et al., 2003), and the top 20 retrieved terms were plotted with both strength (Log10
818 [observed / expected]) and false discovery rate (FDR) (interaction score ≥ 0.7). Terms were clustered
819 through the similarity of enrichment strength patterns across the four groups and the results were further
820 visualized using clusterProfiler 4.0 (Wu et al., 2021; Yu et al., 2012).

821 **PPIs network construction**

822 Differentially enriched proteins under unstimulated or stimulated condition that passed the filtering
823 criteria (log2[FC]≥0.5 or ≤-0.5, FDR≤ 0.05) were separately uploaded to the STRING portal, and
824 physical subnetwork type was chosen to extract the physical (direct) protein-protein associations from
825 the databases. Active interaction sources, including text mining, experiments, and databases, and an
826 interaction score > 0.7 (high confidence interaction) were applied to construct the PPI networks.
827 Markov clustering algorithm (MCL) was used to group the interaction subnetworks with the inflation
828 value of 3.0, resulting in 13 clusters for the stimulated condition and 18 clusters for the unstimulated
829 condition.

830 **SAINT probabilistic scoring for NLRP3 APEX2 PL-MS and AP-MS data**

831 The computational tool, SAINTexpress (Teo et al., 2014)- an updated version of the "Significance
832 Analysis of INTeractome (SAINT)," was utilised to allocate confidence scores to the proximity
833 labelling and AP-MS data. This analysis was conducted via the online Contaminant Repository for
834 Affinity Purification platform at www.crapome.org (Mellacheruvu et al., 2013).

835 **Statistics and reproducibility**

836 Data are presented as mean ± standard error of the mean (SEM). Two-tailed, unpaired student's t test
837 was used for statistical analysis in GraphPad Prism 9. Unless stated, otherwise all quantitative
838 experiments were performed in triplicates and average with SEM reported.

839 **Data availability**

840 The mass spectrometry proteomics data have been deposited to the ProteomeXchange Consortium via
841 the PRIDE (Deutsch et al., 2023; Perez-Riverol et al., 2022) partner repository with the dataset identifier
842 PXD045862.

843 **Acknowledgements**

844 Z.L., A.D., I.V., G.L., X.Z., R.F., T.D. and B.M.K. were supported by the Chinese Academy of Medical
845 Sciences (CAMS) Innovation Fund for Medical Science (CIFMS), China (grant number: 2018-I2M-2-
846 002) awarded to B.M.K., R.F. and T.D. B.M.K. was supported by Pfizer. E.D. was supported by
847 Alzheimer's Research UK Grants ARUK2015DDI-OX. E.J was funded by Wellcome Trust (grant #
848 224040/Z/21/Z). Imaging was performed using the Oxford-Zeiss Centre of Excellent in Biomedical
849 Imaging and the Kennedy Trust for Rheumatology Research (grant # 202117 and 202103, respectively).
850 E.W.T. was supported by a CRUK Programme Award (DRCNPG-Nov21\100001) with support from
851 the Engineering & Physical Sciences Research Council. We would also like to thank members of the
852 Discovery Proteomics Facility, the Kessler, Oxford Drug Discovery Institute groups for constructive
853 discussions and Raphael Heilig for his expert help with mass spectrometry.

854 **Author contributions**

855 B.M.K., E.D. and Z.L. designed the research and wrote the manuscript. Z.L. and A.D. performed the
856 NLRP3-APEX2 proximity labelling experiments and analysed the mass spectrometry data. Z.L. and
857 A.D. performed the DUB siRNA library screen experiment. I.V. operated mass spectrometer for LC-
858 MS/MS acquisition of the samples and contributed to data processing. E.J. performed confocal imaging
859 and analysis. S.J.W. and A.D. contributed to the culture of hiPSC and differentiated them into microglial
860 cells. E.W.T. and F.C. contributed to UCH-L1 inhibitor provision and study design. Z.L., A.D., I.V.,
861 E.J., F.H.L., S.J.W., G.L., G.Y., H.L., F.C., X.Z., R.F., T.D., E.W.T., E.D. and B.M.K discussed the
862 results, commented, and provided critical reviews on the manuscript.

863 **Competing interests**

864 E.W.T. is a founder and shareholder in Myricx Pharma Ltd, and receives consultancy or research
865 funding from Kura Oncology, Pfizer Ltd, Samsara Therapeutics, Myricx Pharma Ltd, MSD, Exscientia
866 and Daiichi Sankyo. The other authors declare no competing interests.

867

868

869

870

871

872

873

874 **Figure S1**

875

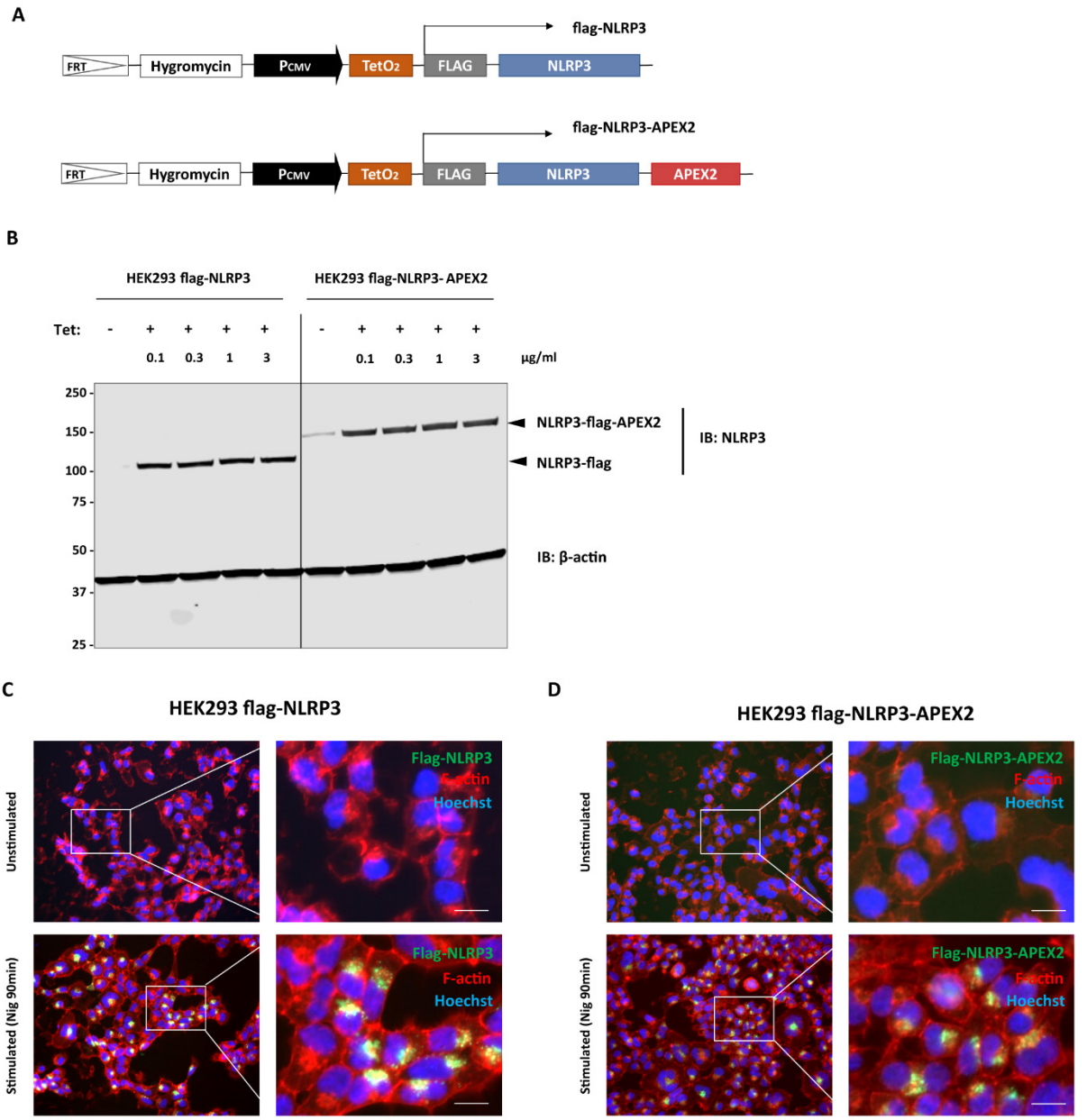

876

877 **Figure S1 | Construction of flag-NLRP3 and flag-NLRP3-APEX2 HEK293 stable cell line**

878 (A) Schematic of Flag-NLRP3 and Flag-NLRP3-APEX2 constructs. (B) Both the flag-NLRP3 and flag-
879 NLRP3-APEX2 Flp-In T-Rex HEK293 stable cell lines were treated with tetracycline at indicated
880 concentrations (0.1-3 μg/mL). 24 hours after induction, cell lysates were collected for immunoblotting
881 analysis. (C-D) Immunofluorescence of flag-NLRP3 (C) and flag-NLRP3-APEX2 (D) in Flp-In T-Rex
882 HEK293 stable cell lines. Cells were either treated with DMSO or Nigericin (10μM) for 90 min. Scale
883 bars, 10 μm.

884

885 **Figure S2**

886

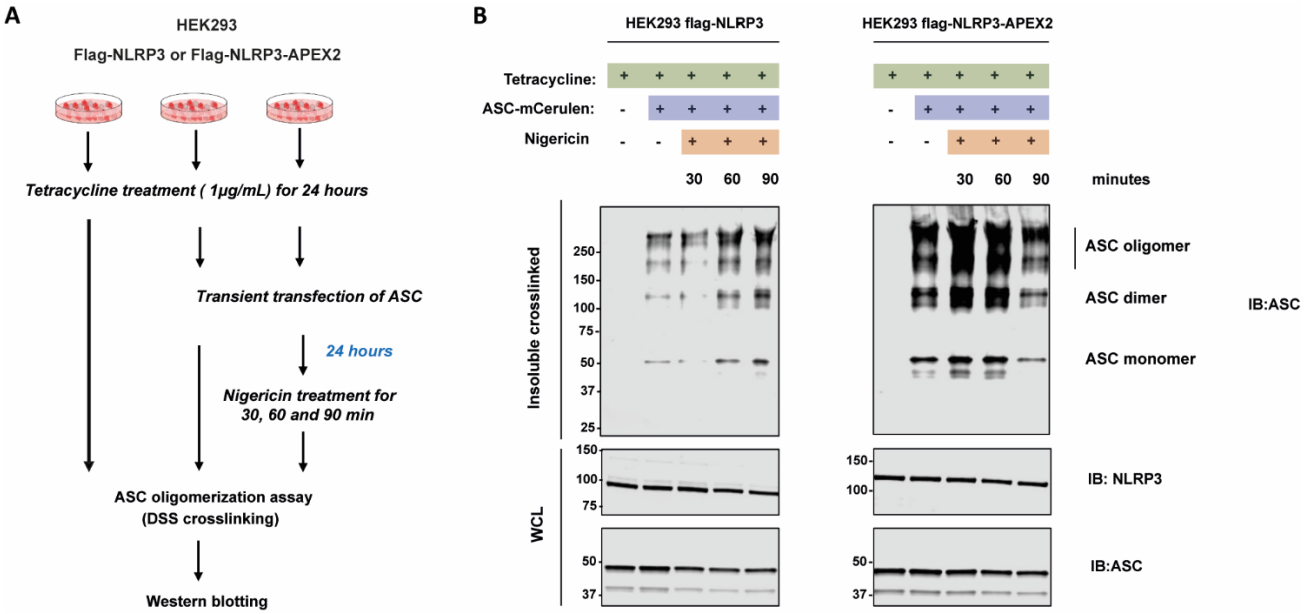

887

888 **Figure S2 | Reconstituted NLRP3 induces ASC oligomerization in HEK293 cell lines**

889 (A) Schematic of the ASC oligomerization assay in Flp-In T-Rex HEK293 stable cell lines. (B)
890 Immunoblot of DSS-crosslinked ASC oligomers in the lysates from flag-NLRP3 and flag-NLRP3-
891 APEX2 HEK293 stable cell lines, treated with tetracycline overnight, transfected with ASC mCerulean,
892 and followed by the treatment with nigericin (10µM) for the indicated time.

893
894
895
896
897
898
899
900
901
902
903
904
905
906
907
908
909

Figure S3

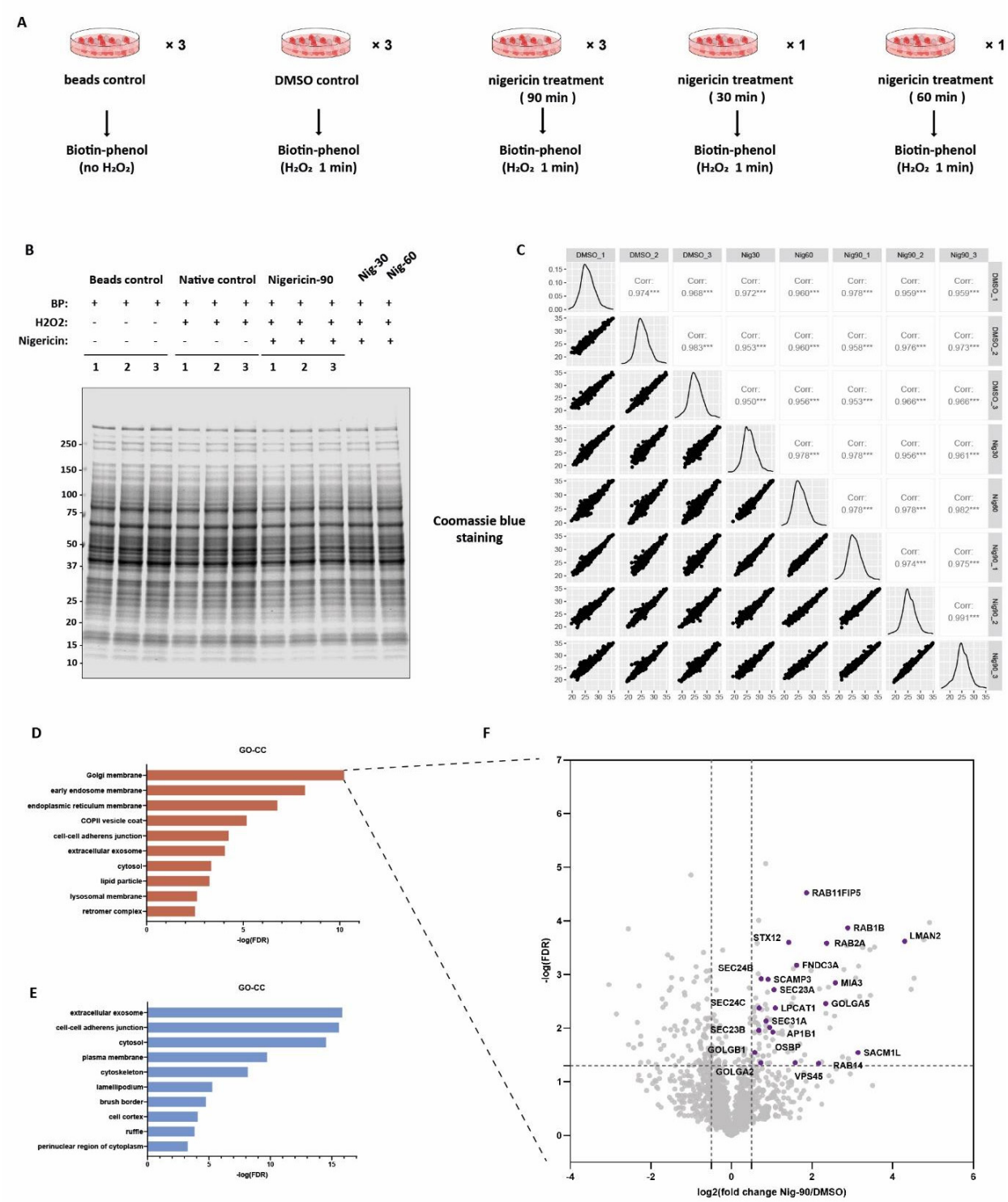

Figure S3 | Tracing NLRP3 translocation using NLRP3-APEX2 proximity labelling

(A) Scheme of the experimental design and procedures of NLRP3-APEX2 proximity labelling. (B) Coomassie blue staining of whole-cell lysates from HEK293 Flp-In T-Rex NLRP3-APEX2 cells, treated as indicated with tetracycline, biotin-phenol, H_2O_2, and nigericin. (C) Pearson correlation matrix heatmap of the biotinylated proteome profiling. This analysis confirms high reproducibility in protein

relative abundance measurements. (D-F) Bar graph showing the top 10 gene ontology-cellular component (GO-CC) terms of the proteins enriched in nigericin-stimulated state (nigericin treatment for 90 min) (D) and unstimulated state (DMSO treatment for 90 min) (E) respectively. (F) The 24 protein that belong to the Golgi membranes term are shown and coloured as purple in the volcano plotting.

944 **Figure S4**

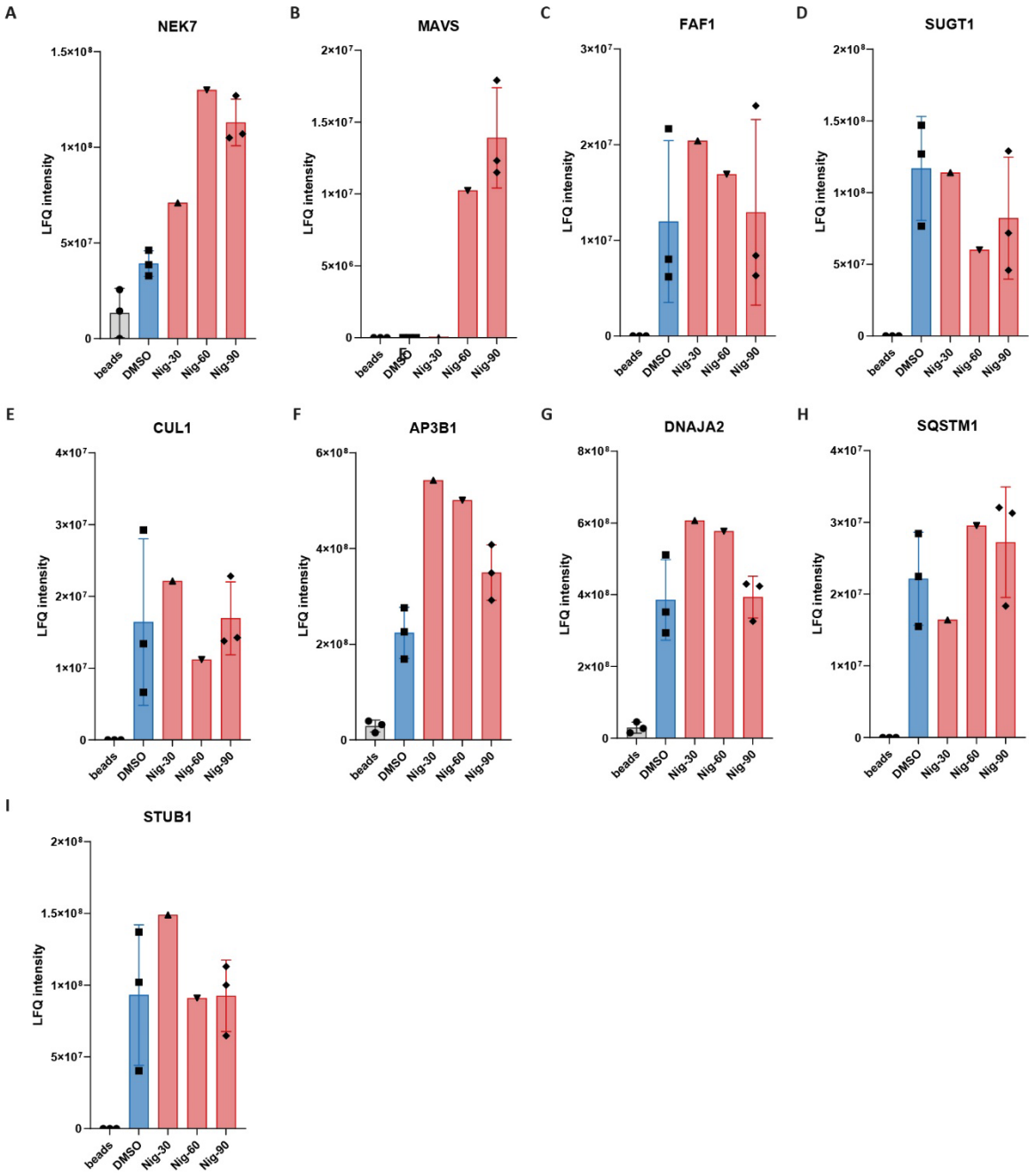

945

946 **Figure S4 | APEX2 proximity labelling identifies known NLRP3-interacting proteins during**
947 **NLRP3 activation downstream of potassium efflux**

948 (A-I) The raw LFQ Intensity values of the APEX2 NLRP3 proximity labelling from all the known
949 NLRP3-interacting proteins identified in our experiment. An average value of 3 independent
950 experiments is presented for DMSO and Nig-90 whereas for Nig-30 and Nig-60 just a single experiment.
951 Error bars show the standard deviation of the mean.

952

953

954 **Figure S5**

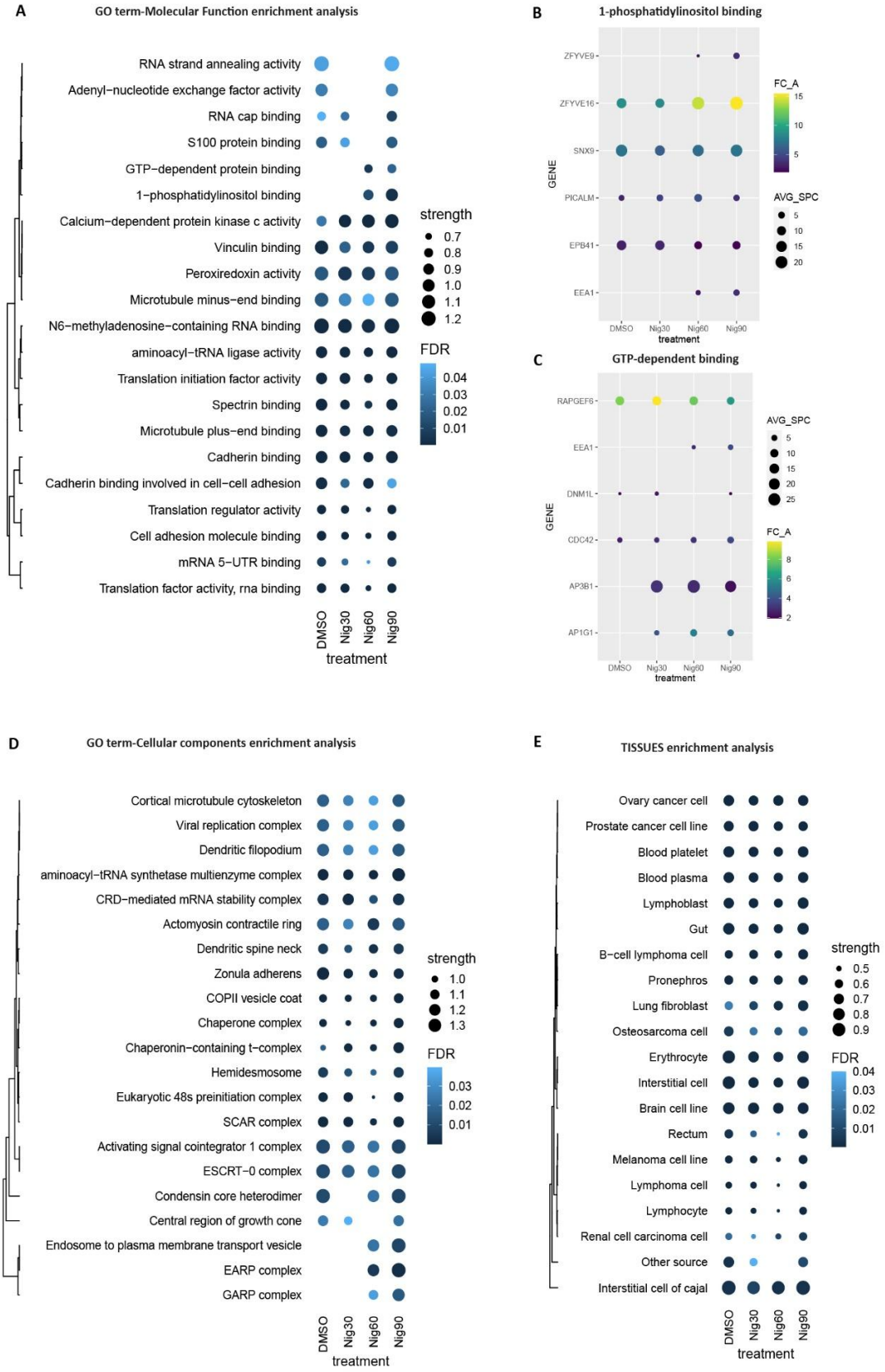

955

956 **Figure S5 | Functional analysis of the NLRP3 proximal proteins during inflammasome activation**

(A, D, E) Dot plots displaying the GOBP (A), GOCC (D) and TISSUE (E) enrichment analysis of high confidence NLRP3 proximal proteins upon nigericin stimulation for different timepoints as indicated. (B, C) Dot plots showing the average spectral counts (AVG_SPC) and fold change (FC_A) of NLRP3 proximal proteins enriched in the GOMF term 1-phosphatidylinostol binding (B) and GTP-dependent binding (C) respectively.

984 **Figure S6**

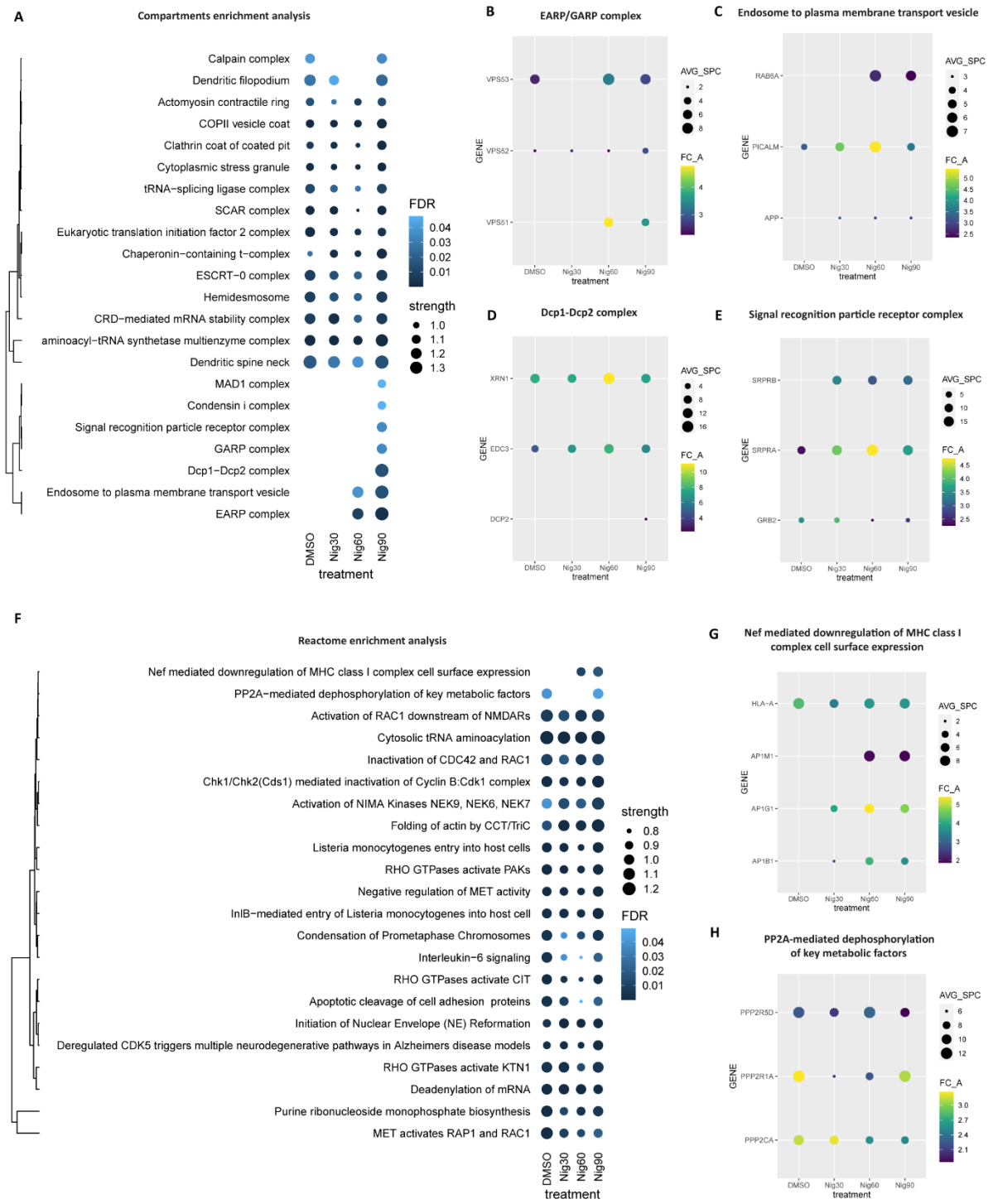

985

986 **Figure S6 | Functional analysis of the NLRP3 proximal proteins during inflammasome activation**
987 (A, D) Dot plots displaying the Compartments (A) and Reactome (F) enrichment analysis of high
988 confidence NLRP3 proximal proteins upon nigericin stimulation for different timepoints. (B-E, G-H)
989 Dot plots showing the average spectral counts (AVG_SPC) and fold change (FC_A) of NLRP3
990 proximal proteins enriched in the term EARP/GARP complex (B), Endosome to plasma membrane
991 transport vesicle (C), Dcp1-Dcp2 complex (D) and Signal recognition particle receptor complex (E),

992 Nef mediated downregulation of MHC class I complex cell surface expression (G), PP2A-mediated
993 dephosphorylation of key metabolic factors (H) respectively.

994

995

996

997

998

999

1000

1001

1002

1003

1004

1005

1006

1007

1008

1009

1010

1011

1012

1013

1014

1015

1016

1017

1018 **Figure S7**

1019

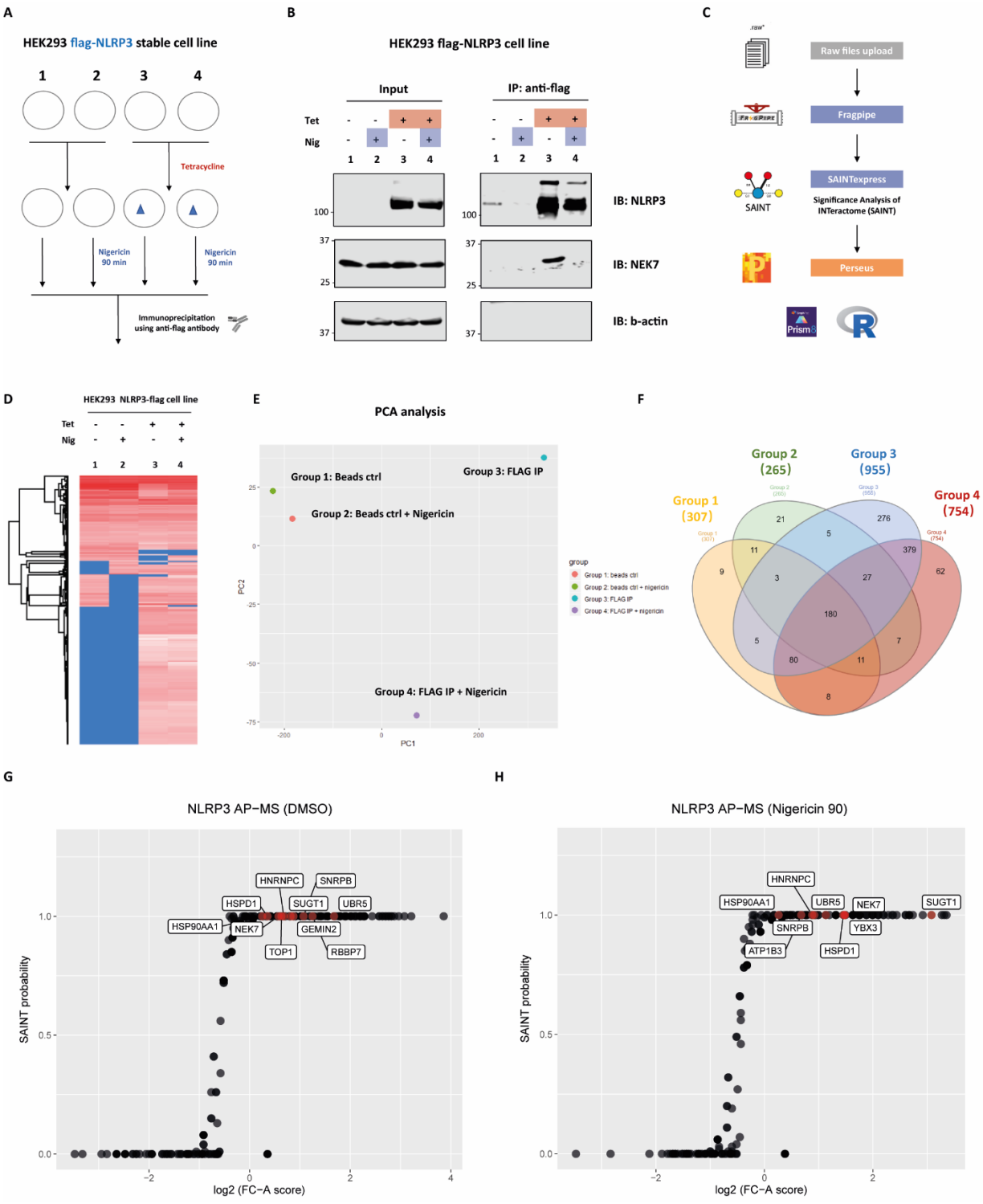

1020

1021

1022 **Figure S7 | NLRP3 interactome determined by AP-MS**

1023 (A) Schematic of the NLRP3 AP-MS experiment design. (B) Stable HEK293 cells expressing Flag-
1024 NLRP3 were incubated with tetracycline overnight. Subsequently, they were treated with nigericin for
1025 90 min as specified. NLRP3-flag was then isolated using an anti-flag antibody and subjected to

immunoblotting with the indicated antibodies. (C) Diagram illustrating the data analysis workflow for AP-MS data. (D) Heatmap showing the hierarchical clusters of prey proteins in the NLRP3 AP-MS across the four groups. (E) Principal component analysis of the four samples. Each dot represents an individual sample. (F) Venn diagram illustrating the number of proteins identified from different groups as indicated in (A). (G-H) SAINT probability scoring of the proteomic data for NLRP3 AP-MS compared to the negative beads control. Proteins passing the cut-off (SAINT probability ≥ 0.8, FC-A ≥ 1) are considered as high-confidence interacting proteins for NLRP3.

1063 **Figure S8**

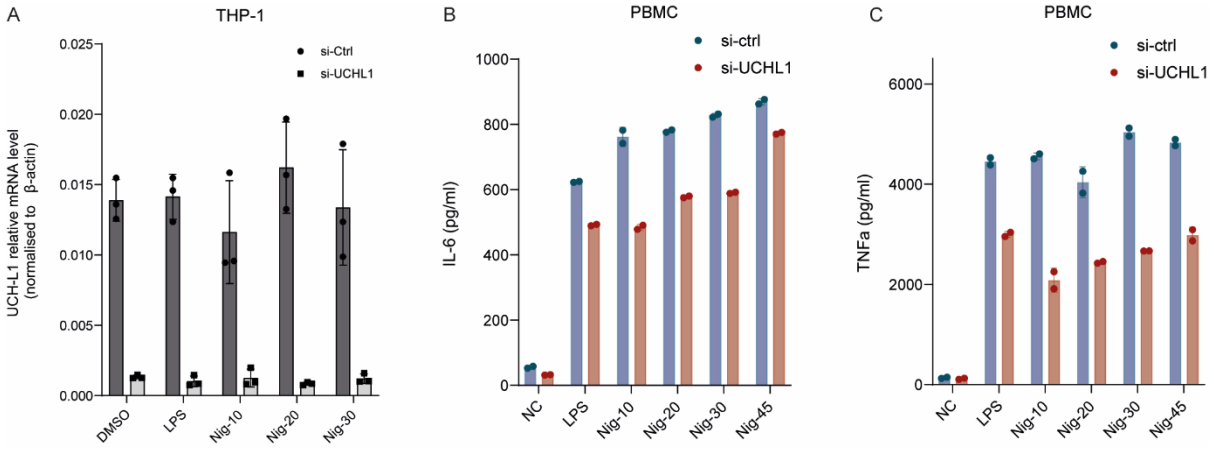

1064

1065 **Figure S8 | UCH-L1 deficiency decreases IL-6 and TNFα expression in human PBMC**

1066 (A) RT-qPCR analysis of UCH-L1 expression in THP-1 cells after transfection with either non-targeting
1067 siRNA or UCH-L1-targeted siRNA. Following differentiation with PMA, cells were primed using LPS
1068 (1 μg/mL) for 4 hours, and then treated with nigericin (10 μM) for different timepoints as indicated. (B-
1069 C) PBMCs were transfected with non-targeting control, or UCH-L1-specific siRNA, stimulated with
1070 LPS for 4 hours and nigericin for different timepoints as indicated. Production of IL-6 (B) and TNFα
1071 (C) in the supernatants from PBMCs were measured by ELISA.

1072
1073
1074
1075
1076
1077
1078
1079
1080
1081
1082
1083
1084
1085
1086
1087
1088
1089
1090

1091 **Figure S9**

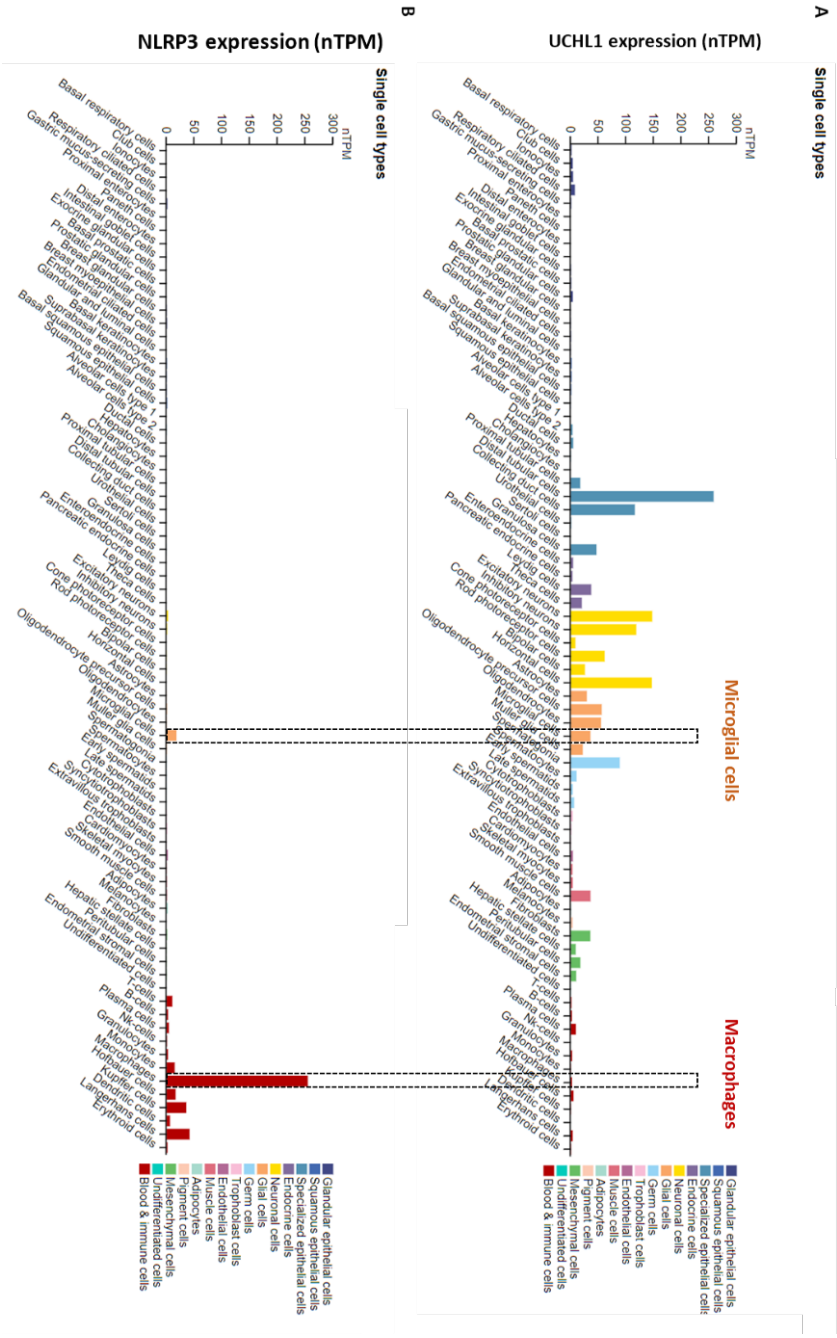

1092

1093

1094 **Figure S9 | RNA expression level of NLRP3 and UCH-L1 in different cell types**

1095 (A,B) A summary of normalized single cell RNA expression (nTPM) in different cell lines for UCH-

1096 L1 (A) and NLRP3 (B). Color-coding represents different cell type groups consisting of cell types with

1097 functional features in common (Data were retrieved from https://www.proteinatlas.org/)

1098

1099

1100 **Figure S10**

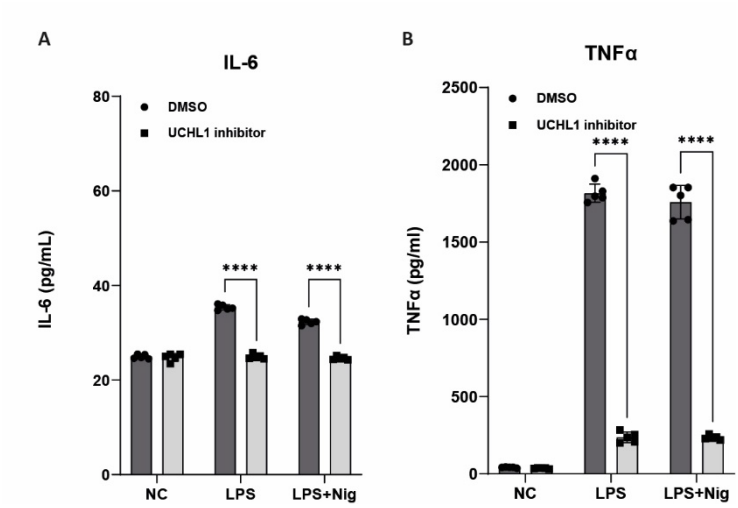

1101

1102 **Figure S10 | UCH-L1 inhibitor diminishes IL-6 and TNFα expression in THP-1 cells**

1103 (A, B) IL-6 (A) and TNFα (B) levels determined by ELISA from THP-1 cells treated with DMSO or
1104 0.3 μM IMP-1711-S. Cells were differentiated with PMA and primed with LPS 1 μg/mL) for 4 hours,
1105 followed by the treatment of nigericin (10 μM) for 45 minutes. The inhibitor or the DMSO were added
1106 at the same time with LPS. Error bars show the standard deviation of the mean. ****$p < 0.0001$
1107 (unpaired two-sided t-test).

1108

1109

1110

1111

1112

1113

1114

1115

1116

1117

1118

1119

1120

1121 **Figure S11**

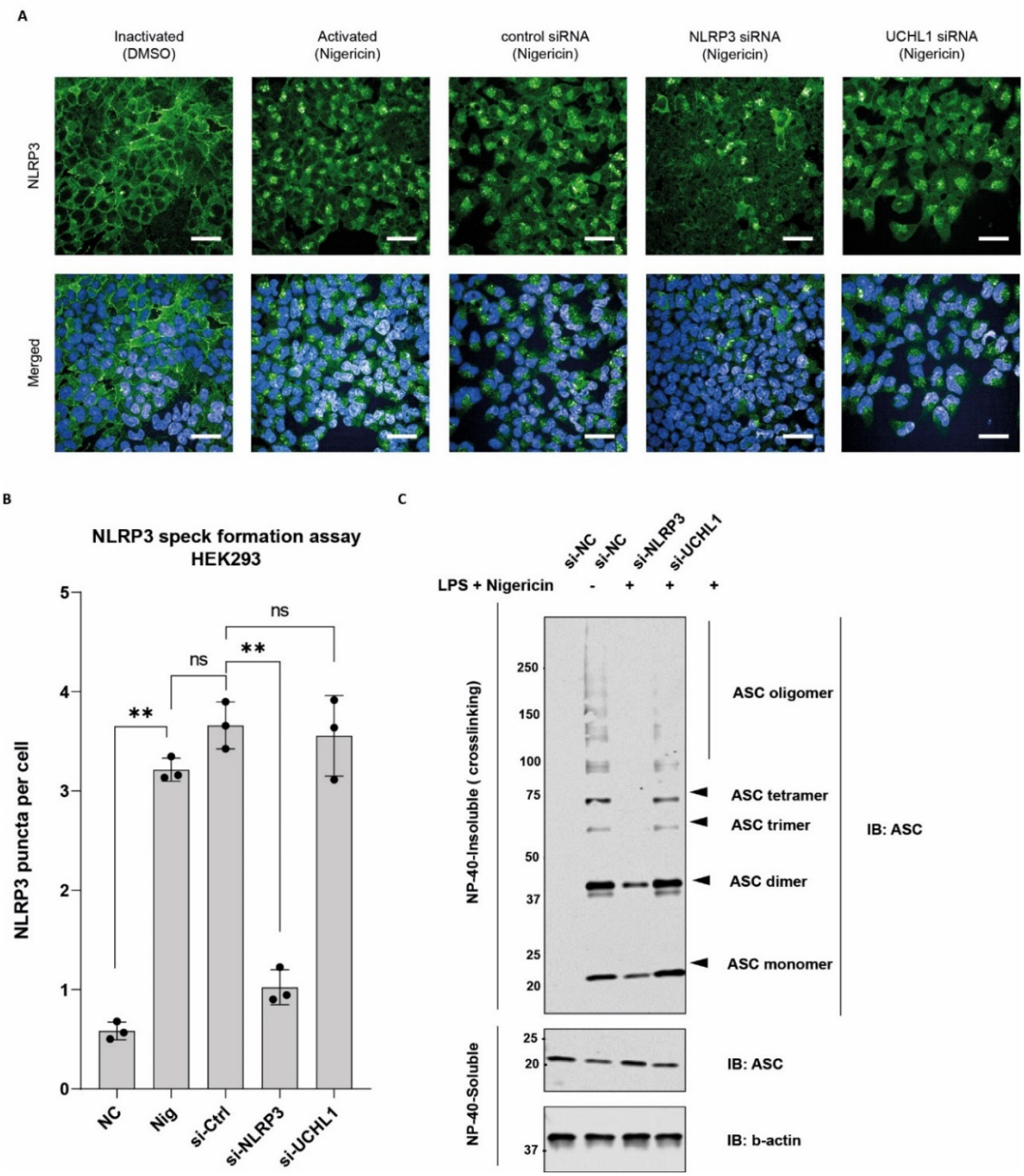

1122

1123 **Figure S11 | UCH-L1 is dispensable for NLRP3 puncta formation but partially alters ASC**
1124 **oligomerization**

1125 (A, B) flag-NLRP3 HEK293 stable cells were transfected with non-targeting control siRNA, NLRP3 or
1126 UCH-L1-specific siRNA. 48 hours after transfection, cells were treated with DMSO or 10 μM nigericin
1127 for 45 minutes. Subsequently, cells were stained with anti-flag antibody to measure the formation of
1128 NLRP3 puncta. (A) Representative fluorescence imaging of NLRP3 puncta using Opera Phenix Plus
1129 High-Content Screening System. Scale bars, 50 μm. (B) Quantitative analysis of the NLRP3 puncta
1130 formation (n = 3, mean ± s.d.). (C) Immunoblot analysis of ASC after DSS crosslinking in THP-1 cells
1131 transfected with non-targeting control siRNA, NLRP3 or UCH-L1-specific siRNA.

1132 **Figure S12**

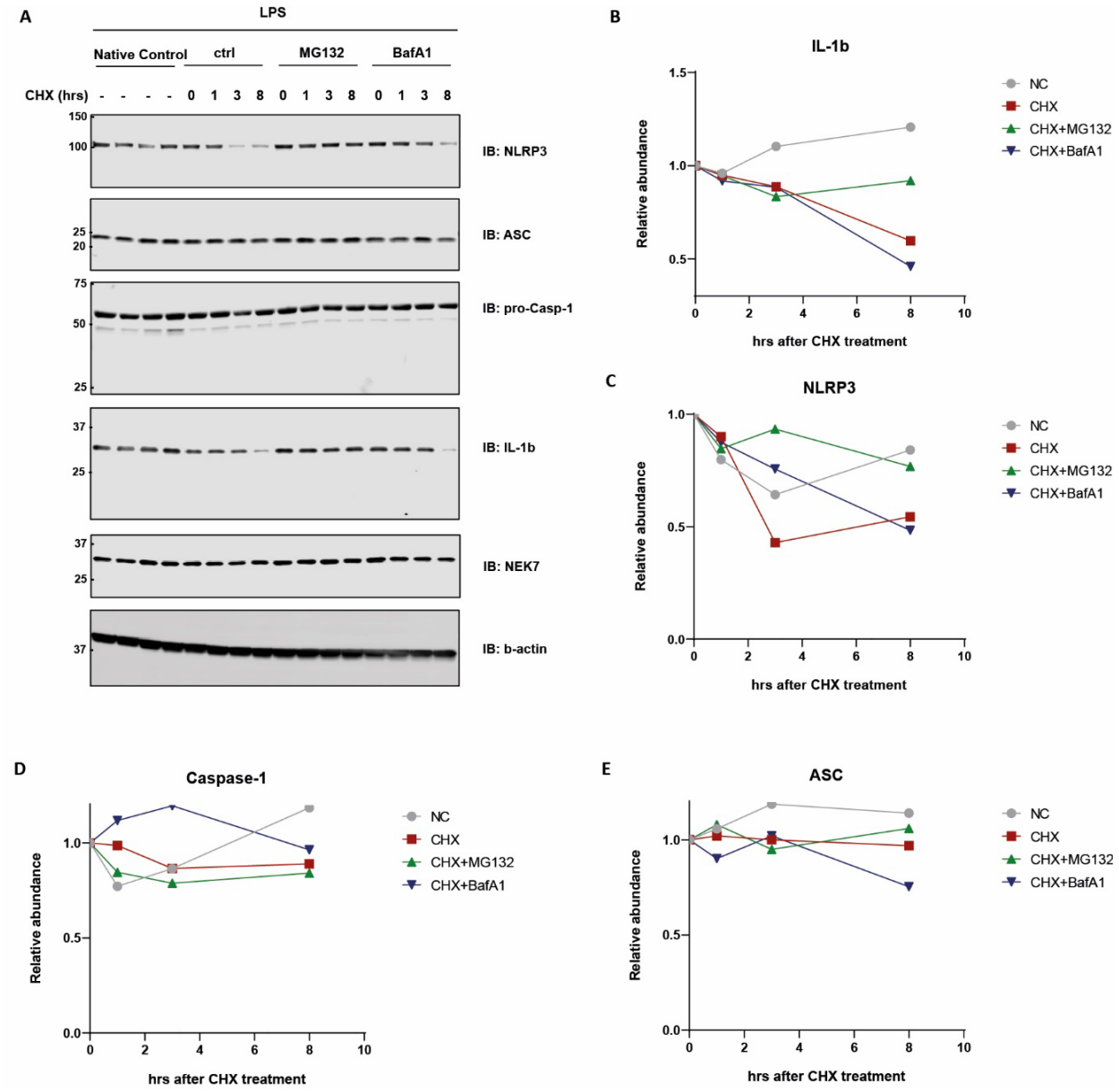

1133

1134

1135 **Figure S12 | Protein turnover of NLRP3 and IL-1β depend on the ubiquitin proteasome pathway**

1136 (A) PMA-differentiated THP-1 cells were primed with LPS (100ng/mL) for 4 hours and followed by
1137 the treatment of MG132 (20μM) or BafA1 (300nM) as indicated in the last 30 min alongside. Cells
1138 were then treated with cycloheximide (50μg/mL) for 1, 3 and 8 h as indicated. Cell lysates were
1139 collected and immunoblotted for the indicated antibodies. Immunoblotting from one representative
1140 experiment of three is shown. (B-E) Quantitative analysis of the western blotting results in (A).

1141

1142

1143 **Figure S13**

1144 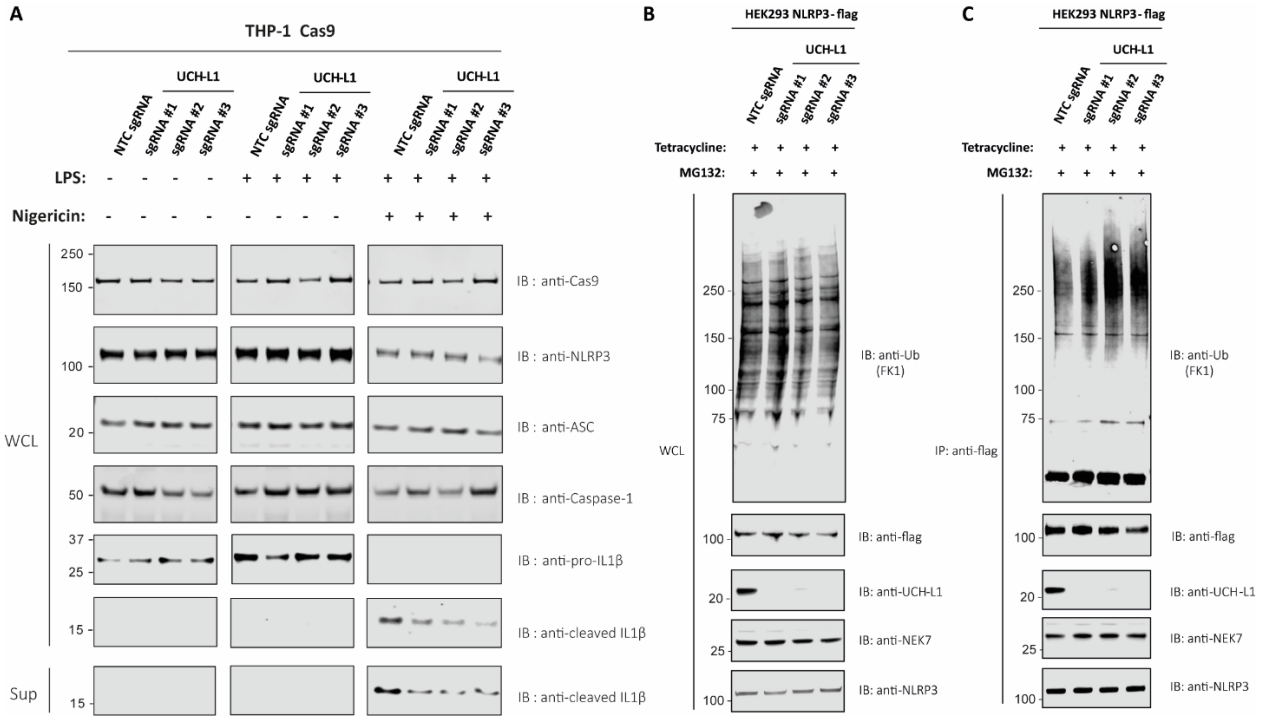

1145 **Figure S13 | UCH-L1 deficiency abrogates IL-1β production and alters NLRP3 ubiquitination**

1146 (A) THP-1 cells, transduced by lentiviruses encoding Cas9 and non-targeting control (NTC) sgRNA or
1147 sgRNA-1/2/3 targeting UCH-L1, were differentiated with PMA, primed with LPS for 4 hours and
1148 treated with nigericin for 45 minutes, as indicated. Whole cell lysates and supernatants were
1149 immunoblotted with indicated antibodies. (B-C) flag-NLRP3 HEK293 stable cell lines, transduced by
1150 lentiviruses encoding Cas9 and non-targeting control (NTC) sgRNA or sgRNA-1/2/3 targeting UCH-
1151 L1, were treated with MG132 (10 μM) for 6 hours. Whole cell lysates (A) and flag-NLRP3
1152 immunoprecipitated in RIPA lysis buffer (B) were analysed with indicated antibodies.

1153

1154

1155

1156

1157

1158

1159

1160

1161 **Table S1 | List of known NLRP3-interacting proteins curated from literature**

1162

Interactor	Experimental System	Throughput	Organism	Reference
HIST1H1B	Affinity Capture-MS	High Throughput	Homo sapiens	PUBMED:26496610
HNRNPC	Affinity Capture-MS	High Throughput	Homo sapiens	PUBMED:26496610
RBBP7	Affinity Capture-MS	High Throughput	Homo sapiens	PUBMED:26496610
SNRPB	Affinity Capture-MS	High Throughput	Homo sapiens	PUBMED:26496610
SPAST	Affinity Capture-MS	High Throughput	Homo sapiens	PUBMED:26496610
TOP1	Affinity Capture-MS	High Throughput	Homo sapiens	PUBMED:26496610
LTBP4	Affinity Capture-MS	High Throughput	Homo sapiens	PUBMED:26496610
SMARCA5	Affinity Capture-MS	High Throughput	Homo sapiens	PUBMED:26496610
GEMIN2	Affinity Capture-MS	High Throughput	Homo sapiens	PUBMED:26496610
YBX3	Affinity Capture-MS	High Throughput	Homo sapiens	PUBMED:26496610
AP3B1	Affinity Capture-MS	High Throughput	Homo sapiens	PUBMED:26496610
PHF14	Affinity Capture-MS	High Throughput	Homo sapiens	PUBMED:26496610
URB1	Affinity Capture-MS	High Throughput	Homo sapiens	PUBMED:26496610
DNAJA2	Affinity Capture-MS	High Throughput	Homo sapiens	PUBMED:26496610
CBX3	Affinity Capture-MS	High Throughput	Homo sapiens	PUBMED:26496610
FBXO28	Affinity Capture-MS	High Throughput	Homo sapiens	PUBMED:26496610
CBX5	Affinity Capture-MS	High Throughput	Homo sapiens	PUBMED:26496610
MTCH1	Affinity Capture-MS	High Throughput	Homo sapiens	PUBMED:26496610
PVRL3	Affinity Capture-MS	High Throughput	Homo sapiens	PUBMED:26496610
FBXL6	Affinity Capture-MS	High Throughput	Homo sapiens	PUBMED:26496610
UQCRQ	Affinity Capture-MS	High Throughput	Homo sapiens	PUBMED:26496610
COPS7A	Affinity Capture-MS	High Throughput	Homo sapiens	PUBMED:26496610
LUC7L3	Affinity Capture-MS	High Throughput	Homo sapiens	PUBMED:26496610
GPATCH4	Affinity Capture-MS	High Throughput	Homo sapiens	PUBMED:26496610
FEM1A	Affinity Capture-MS	High Throughput	Homo sapiens	PUBMED:26496610
LUC7L	Affinity Capture-MS	High Throughput	Homo sapiens	PUBMED:26496610

Interactor	Experimental System	Throughput	Organism	Reference
DMAP1	Affinity Capture-MS	High Throughput	Homo sapiens	PUBMED:26496610
PHRF1	Affinity Capture-MS	High Throughput	Homo sapiens	PUBMED:26496610
CCDC86	Affinity Capture-MS	High Throughput	Homo sapiens	PUBMED:26496610
PCGF5	Affinity Capture-MS	High Throughput	Homo sapiens	PUBMED:26496610
ZC3H8	Affinity Capture-MS	High Throughput	Homo sapiens	PUBMED:26496610
KIAA2013	Affinity Capture-MS	High Throughput	Homo sapiens	PUBMED:26496610
NLRP5	Affinity Capture-MS	High Throughput	Homo sapiens	PUBMED:26496610
STUB1	Affinity Capture-MS	Low Throughput	Homo sapiens	PUBMED:25594175
MARCH7	Affinity Capture-MS	Low Throughput	Homo sapiens	PUBMED:25594175
UBR5	Affinity Capture-MS	Low Throughput	Homo sapiens	PUBMED:25594175
CUL4A	Affinity Capture-MS	High Throughput	Homo sapiens	PUBMED:30945288
CUL4B	Affinity Capture-MS	High Throughput	Homo sapiens	PUBMED:30945288
VDR	Affinity Capture-MS, Affinity Capture-Western, Reconstituted Complex	High Throughput	Homo sapiens	PUBMED:31866999
NLRC4	Affinity Capture-Western	Low Throughput	Homo sapiens	PUBMED:15107016
SUGT1	Affinity Capture-Western	Low Throughput	Homo sapiens	PUBMED:17435760
HSP90AA1	Affinity Capture-Western	Low Throughput	Homo sapiens	PUBMED:17435760
DHX33	Affinity Capture-Western	Low Throughput	Homo sapiens	PUBMED:25172487
ULK1	Affinity Capture-Western	Low Throughput	Homo sapiens	PUBMED:26347139
MEFV	Affinity Capture-Western	Low Throughput	Homo sapiens	PUBMED:26347139
HDAC6	Affinity Capture-Western	Low Throughput	Homo sapiens	PUBMED:26471297
USP50	Affinity Capture-Western	Low Throughput	Homo sapiens	PUBMED:28094437
ARIH2	Affinity Capture-Western	Low Throughput	Homo sapiens	PUBMED:29021376
TXNIP	Affinity Capture-Western, Two-hybrid	Low Throughput	Homo sapiens	PUBMED:28326454, PUBMED:30833078, PUBMED:32323100, PUBMED:32716108
RBX1	Affinity Capture-Western	Low Throughput	Homo sapiens	PUBMED:30653357
FAM175B	Affinity Capture-Western	Low Throughput	Homo sapiens	PUBMED:30787184
BRCC3	Affinity Capture-Western	Low Throughput	Homo sapiens, Mus musculus	PUBMED:30787184, PUBMED:31866999, PUBMED:32941940

Interactor	Experimental System	Throughput	Organism	Reference
ORF8b	Affinity Capture-Western	Low Throughput	Severe acute respiratory syndrome-related coronavirus	PUBMED:31231549
SRC	Affinity Capture-Western	Low Throughput	Homo sapiens	PUBMED:31553908
NEK7	Affinity Capture-Western	Low Throughput	Homo sapiens	PUBMED:31762063, PUBMED:31866999
Ppp2ca	Affinity Capture-Western	Low Throughput	Homo sapiens	PUBMED:31866999
SQSTM1	Affinity Capture-Western	Low Throughput	Homo sapiens	PUBMED:32003754
IL1B	Affinity Capture-Western	Low Throughput	Homo sapiens	PUBMED:32597834
EIF3F	Affinity Capture-Western	Low Throughput	Homo sapiens	PUBMED:33243234
USP13	Affinity Capture-Western	Low Throughput	Homo sapiens	PUBMED:33243234
PSMB8	Affinity Capture-Western	Low Throughput	Homo sapiens	PUBMED:32782149
PARK2	Affinity Capture-Western	Low Throughput	Homo sapiens	PUBMED:33527027
BTRC	Affinity Capture-Western	Low Throughput	Homo sapiens	PUBMED:33976226
TRIM24	Affinity Capture-Western	Low Throughput	Homo sapiens	PUBMED:33724611
USP5	Affinity Capture-Western	Low Throughput	Homo sapiens	PUBMED:34486483
TRIM28	Affinity Capture-Western	Low Throughput	Homo sapiens	PUBMED:34373456
LYN	Affinity Capture-Western	Low Throughput	Homo sapiens	PMID: 34699250
EIF2AK2	Affinity Capture-Western	Low Throughput	Homo sapiens	PMID: 22801494
PRKD1/2/3	Affinity Capture-Western	Low Throughput	Homo sapiens	PMID: 28716882
FBXL2	Affinity Capture-Western, Biochemical Activity	Low Throughput	Homo sapiens	PUBMED:26037928
PYCARD	Affinity Capture-Western, Co-localization	Low Throughput	Homo sapiens	PUBMED:30182366, PUBMED:32003754, PUBMED:32435622
P2RY2	Affinity Capture-Western, Co-localization	Low Throughput	Homo sapiens	PUBMED:31553908
MAVS	Affinity Capture-Western, Co-localization	Low Throughput	Homo sapiens	PMID: 23582325
NLRP11	Affinity Capture-Western, Co-localization	Low Throughput	Homo sapiens	PMID: 35624206
CBLB	Affinity Capture-Western, Reconstituted Complex	Low Throughput	Homo sapiens	PUBMED:31999304

Interactor	Experimental System	Throughput	Organism	Reference
RNF125	Affinity Capture-Western, Reconstituted Complex	Low Throughput	Homo sapiens	PUBMED:31999304
STAMBP	Biochemical Activity, Affinity Capture-Western	Low Throughput	Homo sapiens	PUBMED:32003754, PUBMED:33253913
MCFD2	Co-fractionation	High Throughput	Homo sapiens	PUBMED:26344197
ARHGAP17	Co-fractionation	High Throughput	Homo sapiens	PUBMED:26344197
SH3BP1	Co-fractionation	High Throughput	Homo sapiens	PUBMED:26344197
CASP8	Co-localization	Low Throughput	Homo sapiens	PUBMED:30182366
MARK4	Co-localization	Low Throughput	Homo sapiens	PUBMED:31167564
HSPD1	Proximity Label-MS	High Throughput	Homo sapiens	PUBMED:30021884
Rnf213	Reconstituted Complex	High Throughput	Homo sapiens, Mus musculus	PUBMED:31999304
Trim21	Reconstituted Complex	High Throughput	Homo sapiens, Mus musculus	PUBMED:31999304
Trim47	Reconstituted Complex	High Throughput	Homo sapiens, Mus musculus	PUBMED:31999304
Trim14	Reconstituted Complex	High Throughput	Homo sapiens, Mus musculus	PUBMED:31999304
ORF8	Reconstituted Complex, Affinity Capture-Western	Low Throughput	Severe acute respiratory syndrome coronavirus 2	DOI:10.1101/2021.12.02.470978
TRIM31	Reconstituted Complex, Affinity Capture-Western, Biochemical Activity	Low Throughput	Homo sapiens	PUBMED:27929086
PGM1	Two-hybrid	High Throughput	Homo sapiens	PUBMED:30653357
ATP1B3	Two-hybrid	High Throughput	Homo sapiens	PUBMED:30653357
CUL1	Two-hybrid, Affinity Capture-Western, Co-localization, PCA	High Throughput	Homo sapiens	PUBMED:30653357
PXN	Two-hybrid, Affinity Capture-Western, Reconstituted Complex, Co-localization	Low Throughput	Homo sapiens	PUBMED:33243234
FAF1	Two-hybrid, Reconstituted Complex, Affinity Capture-Western	Low Throughput	Homo sapiens	PUBMED:17046979

1167 **Table S2 | List of the Golgi membrane proteins differentially captured by NLRP3-APEX2 during**
1168 **nigericin-induced inflammasome assembly**

Protein IDs	Protein names	Gene names	Peptides	Unique peptides	Sequence coverage [%]
O14828	Secretory carrier-associated membrane protein 3	SCAMP3	11	11	42.1
O94979	Protein transport protein Sec31A	SEC31A	26	26	23
O95487	Protein transport protein Sec24B	SEC24B	23	23	22.7
P22059	Oxysterol-binding protein 1	OSBP	20	20	33
P53992	Protein transport protein Sec24C	SEC24C	25	24	31.9
P61019;Q8WUD1	Ras-related protein Rab-2A;Ras-related protein Rab-2B	RAB2A;RAB2B	6	6	37.7
P61106	Ras-related protein Rab-14	RAB14	12	12	65.6
Q00610	Clathrin heavy chain 1	CLTC	57	57	39.6
Q08379	Golgin subfamily A member 2	GOLGA2	22	22	28
Q10567	AP-1 complex subunit beta-1	AP1B1	19	5	21.6
Q12907	Vesicular integral-membrane protein VIP36	LMAN2	11	11	37.9
Q14789	Golgin subfamily B member 1	GOLGB1	106	106	45.4
Q15436	Protein transport protein Sec23A	SEC23A	20	17	35.7
Q15437	Protein transport protein Sec23B	SEC23B	24	21	37.2
Q86Y82	Syntaxin-12	STX12	8	8	37.7
Q8NF37	Lysophosphatidylcholine acyltransferase 1	LPCAT1	4	4	10.7
Q8TBA6	Golgin subfamily A member 5	GOLGA5	22	22	41.9
Q9BXF6	Rab11 family-interacting protein 5	RAB11FIP5	12	12	32.3
Q9H0U4;Q92928	Ras-related protein Rab-1B;Putative Ras-related protein Rab-1C	RAB1B;RAB1C	4	2	29.4
Q9NRW7	Vacuolar protein sorting-associated protein 45	VPS45	11	11	19.6
Q9NTJ5	Phosphatidylinositide phosphatase SAC1	SACM1L	11	11	19.3
Q9Y2H6	Fibronectin type-III domain-containing protein 3A	FNDC3A	7	7	8.3

1169

1170

1171

1172

1173 **Table S3 | Human DUB siRNA screening in THP-1 cells**

LPS

Rank	Gene	Normalized IL1b	z-score
1	TNFAIP3	2.334	3.451
2	UCHL3	2.217	2.720
3	CYLD	2.103	2.013
4	USP8	2.016	1.470
5	JOSD2	2.010	1.432
6	USP38	1.996	1.343
7	USP18	1.992	1.320
8	JOSD1	1.992	1.319
9	USP40	1.983	1.261
10	OTUD6B	1.977	1.228
11	ZRANB1	1.976	1.221
12	OTUD7A	1.967	1.162
13	OTUD7B	1.956	1.098
14	USP33	1.951	1.066
15	USP46	1.938	0.984
16	USP43	1.923	0.892
17	STAMBPL1	1.914	0.838
18	OTUB2	1.902	0.759
19	USPL1	1.900	0.746
20	OTUD5	1.898	0.736
21	USP21	1.895	0.715
22	USP48	1.893	0.704
23	USP3	1.870	0.563
24	STAMBP	1.867	0.542
25	USP45	1.863	0.518
26	USP27X	1.863	0.518
27	USP11	1.860	0.501
28	USP13	1.856	0.472
29	COPS5	1.854	0.464
30	USP6	1.848	0.422
31	MYSM1	1.845	0.403
32	USP50	1.838	0.361
33	PAN2	1.832	0.326
34	SENP2	1.832	0.323
35	USP5	1.831	0.317
36	USP24	1.831	0.315
37	PRPF8	1.821	0.259
38	UFD1L	1.816	0.226
39	USP1	1.814	0.214
40	VCPIP1	1.813	0.208
41	PSMD14	1.811	0.197
42	UBL4A	1.801	0.131
43	UCHL5	1.800	0.123

LPS + Nigericin

Rank	Gene	Normalized IL1b	z-score
1	STAMBP	3.064	2.238
2	USP39	2.966	2.015
3	ZRANB1	2.924	1.917
4	USP17L2	2.899	1.861
5	USP38	2.875	1.806
6	USP47	2.846	1.740
7	USP25	2.846	1.739
8	UBTD1	2.794	1.620
9	UCK2	2.775	1.576
10	UCHL3	2.727	1.465
11	COPS5	2.698	1.399
12	USP14	2.689	1.379
13	USP8	2.687	1.375
14	USP33	2.665	1.323
15	ATXN3	2.656	1.304
16	USP31	2.608	1.194
17	UBTD2	2.606	1.187
18	USP37	2.518	0.986
19	USP43	2.515	0.981
20	OTUD1	2.514	0.976
21	USP34	2.505	0.957
22	USP5	2.476	0.890
23	FBXO8	2.452	0.834
24	USP3	2.449	0.828
25	USP22	2.433	0.792
26	STAMBPL1	2.397	0.709
27	BRCC3	2.389	0.691
28	USP42	2.366	0.637
29	USP32	2.357	0.617
30	USP24	2.340	0.579
31	USPL1	2.320	0.532
32	YOD1	2.315	0.521
33	USP54	2.313	0.516
34	JOSD2	2.293	0.471
35	UCHL5	2.272	0.422
36	USP30	2.254	0.381
37	USP40	2.237	0.342
38	USP27X	2.233	0.332
39	USP26	2.206	0.271
40	PRPF8	2.200	0.258
41	UFD1L	2.189	0.233
42	USP35	2.184	0.220
43	OTUD4	2.153	0.150

LPS

Rank	Gene	Normalized IL1b	z-score
44	UBTD2	1.796	0.102
45	USP39	1.791	0.067
46	USP29	1.789	0.059
47	BRCC3	1.785	0.032
48	USP28	1.767	-0.077
49	USP32	1.763	-0.107
50	USP19	1.754	-0.164
51	USP7	1.752	-0.173
52	USP41	1.748	-0.200
53	MPND	1.745	-0.214
54	USP34	1.744	-0.220
55	UBTD1	1.738	-0.260
56	USP4	1.738	-0.262
57	USP10	1.736	-0.273
58	USP25	1.730	-0.307
59	USP44	1.729	-0.317
60	USP9Y	1.729	-0.317
61	FBXO8	1.722	-0.362
62	USP12	1.721	-0.368
63	YOD1	1.721	-0.369
64	USP15	1.718	-0.388
65	UBL5	1.716	-0.397
66	USP22	1.715	-0.405
67	PARP11	1.714	-0.408
68	USP30	1.713	-0.416
69	USP49	1.710	-0.436
70	UEVLD	1.710	-0.437
71	OTUB1	1.699	-0.501
72	USP17L2	1.692	-0.545
73	ATXN3	1.690	-0.557
74	UBL3	1.689	-0.563
75	USP47	1.683	-0.603
76	USP14	1.680	-0.619
77	USP42	1.680	-0.622
78	USP54	1.678	-0.634
79	FBXO7	1.672	-0.671
80	USP35	1.660	-0.743
81	USP16	1.657	-0.765
82	USP53	1.654	-0.781
83	USP2	1.654	-0.782
84	USP31	1.626	-0.956
85	BAP1	1.626	-0.959
86	USP51	1.617	-1.017
87	USP37	1.616	-1.022
88	OTUD1	1.578	-1.258

LPS + Nigericin

Rank	Gene	Normalized IL1b	z-score
44	USP15	2.146	0.133
45	USP36	2.126	0.087
46	PARP11	2.098	0.023
47	USP18	2.082	-0.014
48	USP2	2.063	-0.058
49	PAN2	1.986	-0.234
50	UBL5	1.869	-0.501
51	USP1	1.862	-0.518
52	BAP1	1.826	-0.601
53	USP48	1.822	-0.609
54	SENP2	1.814	-0.627
55	USP9Y	1.796	-0.670
56	OTUD6B	1.796	-0.670
57	FBXO7	1.792	-0.679
58	USP16	1.785	-0.694
59	USP21	1.777	-0.712
60	USP29	1.769	-0.733
61	USP50	1.753	-0.768
62	UBL4A	1.747	-0.781
63	USP46	1.741	-0.795
64	CYLD	1.739	-0.800
65	USP28	1.739	-0.801
66	USP45	1.736	-0.808
67	OTUB2	1.730	-0.820
68	MYSM1	1.726	-0.829
69	USP49	1.715	-0.855
70	USP12	1.714	-0.858
71	UBL3	1.683	-0.930
72	USP44	1.679	-0.938
73	OTUD7A	1.675	-0.948
74	TNFAIP3	1.668	-0.963
75	PSMD14	1.667	-0.965
76	USP20	1.664	-0.972
77	USP41	1.664	-0.972
78	USP4	1.664	-0.973
79	USP19	1.660	-0.981
80	MPND	1.660	-0.981
81	OTUD5	1.658	-0.987
82	USP9X	1.657	-0.989
83	USP53	1.654	-0.996
84	USP13	1.648	-1.010
85	JOSD1	1.647	-1.011
86	VCPIP1	1.640	-1.028
87	USP7	1.622	-1.068
88	UCHL1	1.617	-1.079

LPS

Rank	Gene	Normalized IL1b	z-score
89	OTUD4	1.577	-1.262
90	UBR1	1.520	-1.617
91	UCK2	1.513	-1.663
92	USP9X	1.483	-1.845
93	USP20	1.453	-2.034
94	USP36	1.447	-2.074
95	UCHL1	1.413	-2.286
96	USP26	1.316	-2.887

LPS + Nigericin

Rank	Gene	Normalized IL1b	z-score
89	UEVLD	1.617	-1.081
90	OTUB1	1.613	-1.088
91	USP11	1.605	-1.108
92	USP51	1.600	-1.118
93	OTUD7B	1.587	-1.149
94	UBR1	1.548	-1.238
95	USP6	1.547	-1.240
96	USP10	1.539	-1.259

References

Akther, M., Haque, M.E., Park, J., Kang, T.B., and Lee, K.H. (2021). NLRP3 Ubiquitination-A New Approach to Target NLRP3 Inflammasome Activation. Int J Mol Sci *22*.

Bednash, J.S., Johns, F., Patel, N., Smail, T.R., Londino, J.D., and Mallampalli, R.K. (2021). The deubiquitinase STAMBP modulates cytokine secretion through the NLRP3 inflammasome. Cell Signal *79*, 109859.

Bordon, Y. (2019). Trans-Golgi network breaks away to activate NLRP3. Nat Rev Immunol *19*, 68-69.

Bruntraeger, M., Byrne, M., Long, K., and Bassett, A.R. (2019). Editing the Genome of Human Induced Pluripotent Stem Cells Using CRISPR/Cas9 Ribonucleoprotein Complexes. Methods Mol Biol *1961*, 153-183.

Cao, D.Y., Zhang, Z.H., Li, R.Z., Shi, X.K., Xi, R.Y., Zhang, G.L., Li, F., and Wang, F. (2022). A small molecule inhibitor of caspase-1 inhibits NLRP3 inflammasome activation and pyroptosis to alleviate gouty inflammation. Immunol Lett *244*, 28-39.

Chen, J., and Chen, Z.J. (2018). PtdIns4P on dispersed trans-Golgi network mediates NLRP3 inflammasome activation. Nature *564*, 71-76.

Davis, S., Charles, P.D., He, L., Mowlds, P., Kessler, B.M., and Fischer, R. (2017). Expanding Proteome Coverage with CHarge Ordered Parallel Ion aNalysis (CHOPIN) Combined with Broad Specificity Proteolysis. J Proteome Res *16*, 1288-1299.

Deutsch, E.W., Bandeira, N., Perez-Riverol, Y., Sharma, V., Carver, J.J., Mendoza, L., Kundu, D.J., Wang, S., Bandla, C., Kamatchinathan, S.*, et al.* (2023). The ProteomeXchange consortium at 10 years: 2023 update. Nucleic Acids Res *51*, D1539-D1548.

Duong, B.H., Onizawa, M., Oses-Prieto, J.A., Advincula, R., Burlingame, A., Malynn, B.A., and Ma, A. (2015). A20 restricts ubiquitination of pro-interleukin-1beta protein complexes and suppresses NLRP3 inflammasome activity. Immunity *42*, 55-67.

Fox, D., and Man, S.M. (2019). DDX3X: stressing the NLRP3 inflammasome. Cell Res *29*, 969-970.

Gross, O., Yazdi, A.S., Thomas, C.J., Masin, M., Heinz, L.X., Guarda, G., Quadroni, M., Drexler, S.K., and Tschopp, J. (2012). Inflammasome activators induce interleukin-1alpha secretion via distinct pathways with differential requirement for the protease function of caspase-1. Immunity *36*, 388-400.

Guo, Y., Li, L., Xu, T., Guo, X., Wang, C., Li, Y., Yang, Y., Yang, D., Sun, B., Zhao, X.*, et al.* (2020). HUWE1 mediates inflammasome activation and promotes host defense against bacterial infection. J Clin Invest *130*, 6301-6316.

Hai, B., Mao, T., Du, C., Jia, F., Liu, Y., Song, Q., Pan, X., Liu, X., and Zhu, B. (2022). USP14 promotes pyroptosis of human annulus fibrosus cells derived from patients with intervertebral disc degeneration through deubiquitination of NLRP3. Acta Biochim Biophys Sin (Shanghai) *54*, 1-11.

Ham, S.J., Lee, D., Xu, W.J., Cho, E., Choi, S., Min, S., Park, S., and Chung, J. (2021). Loss of UCHL1 rescues the defects related to Parkinson's disease by suppressing glycolysis. Sci Adv *7*.

Hamilton, C., and Anand, P.K. (2019). Right place, right time: localisation and assembly of the NLRP3 inflammasome. F1000Res *8*.

He, Y., Zeng, M.Y., Yang, D., Motro, B., and Nunez, G. (2016). NEK7 is an essential mediator of NLRP3 activation downstream of potassium efflux. Nature *530*, 354-357.

Huang, Y., He, S., Chen, Y., Sheng, J., Fu, Y., Du, X., Yang, Y., Liu, H., Han, Z., Huang, Y.*, et al.* (2022). UCHL1 Promoted Polarization of M1 Macrophages by Regulating the PI3K/AKT Signaling Pathway. J Inflamm Res *15*, 735-746.

Kummari, E., Alugubelly, N., Hsu, C.Y., Dong, B., Nanduri, B., and Edelmann, M.J. (2015). Activity-Based Proteomic Profiling of Deubiquitinating Enzymes in Salmonella-Infected Macrophages Leads to Identification of Putative Function of UCH-L5 in Inflammasome Regulation. PLoS One *10*, e0135531.

Lambert, J.P., Tucholska, M., Go, C., Knight, J.D., and Gingras, A.C. (2015). Proximity biotinylation and affinity purification are complementary approaches for the interactome mapping of chromatin-associated protein complexes. J Proteomics *118*, 81-94.

1243 Lawlor, K.E., Khan, N., Mildenhall, A., Gerlic, M., Croker, B.A., D'Cruz, A.A., Hall, C., Kaur Spall, S.,
1244 Anderton, H., Masters, S.L.*, et al.* (2015). RIPK3 promotes cell death and NLRP3 inflammasome
1245 activation in the absence of MLKL. Nat Commun *6*, 6282.
1246 Liang, Z., Damianou, A., Di Daniel, E., and Kessler, B.M. (2021). Inflammasome activation controlled by
1247 the interplay between post-translational modifications: emerging drug target opportunities. Cell
1248 Commun Signal *19*, 23.
1249 Liu, Y., Fallon, L., Lashuel, H.A., Liu, Z., and Lansbury, P.T., Jr. (2002). The UCH-L1 gene encodes two
1250 opposing enzymatic activities that affect alpha-synuclein degradation and Parkinson's disease
1251 susceptibility. Cell *111*, 209-218.
1252 Lopez-Castejon, G. (2020). Control of the inflammasome by the ubiquitin system. FEBS J *287*, 11-26.
1253 Lopez-Castejon, G., and Edelmann, M.J. (2016). Deubiquitinases: Novel Therapeutic Targets in
1254 Immune Surveillance? Mediators Inflamm *2016*, 3481371.
1255 Lopez-Castejon, G., Luheshi, N.M., Compan, V., High, S., Whitehead, R.C., Flitsch, S., Kirov, A.,
1256 Prudovsky, I., Swanton, E., and Brough, D. (2013). Deubiquitinases regulate the activity of caspase-1
1257 and interleukin-1beta secretion via assembly of the inflammasome. J Biol Chem *288*, 2721-2733.
1258 Mark Kemp, M.S., Alison Jones (2017). Cyanopyrrolidines as Dub Inhibitors for the Treatment of
1259 Cancer.
1260 Martinon, F., Burns, K., and Tschopp, J. (2002). The inflammasome: a molecular platform triggering
1261 activation of inflammatory caspases and processing of proIL-beta. Mol Cell *10*, 417-426.
1262 Mellacheruvu, D., Wright, Z., Couzens, A.L., Lambert, J.P., St-Denis, N.A., Li, T., Miteva, Y.V., Hauri, S.,
1263 Sardiu, M.E., Low, T.Y.*, et al.* (2013). The CRAPome: a contaminant repository for affinity purification-
1264 mass spectrometry data. Nat Methods *10*, 730-736.
1265 Mondal, M., Conole, D., Nautiyal, J., and Tate, E.W. (2022a). UCHL1 as a novel target in breast cancer:
1266 emerging insights from cell and chemical biology. Brit J Cancer *126*, 24-33.
1267 Mondal, M., Conole, D., Nautiyal, J., and Tate, E.W. (2022b). UCHL1 as a novel target in breast cancer:
1268 emerging insights from cell and chemical biology. Br J Cancer *126*, 24-33.
1269 Olie, C.S., Pinto-Fernandez, A., Damianou, A., Vendrell, I., Mei, H., den Hamer, B., van der Wal, E., de
1270 Greef, J.C., Raz, V., and Kessler, B.M. (2023). USP18 is an essential regulator of muscle cell
1271 differentiation and maturation. Cell Death Dis *14*, 231.
1272 Oughtred, R., Rust, J., Chang, C., Breitkreutz, B.J., Stark, C., Willems, A., Boucher, L., Leung, G., Kolas,
1273 N., Zhang, F.*, et al.* (2021). The BioGRID database: A comprehensive biomedical resource of curated
1274 protein, genetic, and chemical interactions. Protein Sci *30*, 187-200.
1275 Oughtred, R., Stark, C., Breitkreutz, B.J., Rust, J., Boucher, L., Chang, C., Kolas, N., O'Donnell, L., Leung,
1276 G., McAdam, R.*, et al.* (2019). The BioGRID interaction database: 2019 update. Nucleic Acids Res *47*,
1277 D529-D541.
1278 Palazon-Riquelme, P., Worboys, J.D., Green, J., Valera, A., Martin-Sanchez, F., Pellegrini, C., Brough, D.,
1279 and Lopez-Castejon, G. (2018). USP7 and USP47 deubiquitinases regulate NLRP3 inflammasome
1280 activation. EMBO Rep *19*.
1281 Paludan, S.R., Pradeu, T., Masters, S.L., and Mogensen, T.H. (2021). Constitutive immune mechanisms:
1282 mediators of host defence and immune regulation. Nat Rev Immunol *21*, 137-150.
1283 Panicker, N., Sarkar, S., Harischandra, D.S., Neal, M., Kam, T.I., Jin, H., Saminathan, H., Langley, M.,
1284 Charli, A., Samidurai, M.*, et al.* (2019). Fyn kinase regulates misfolded alpha-synuclein uptake and
1285 NLRP3 inflammasome activation in microglia. J Exp Med *216*, 1411-1430.
1286 Panyain, N., Godinat, A., Lanyon-Hogg, T., Lachiondo-Ortega, S., Will, E.J., Soudy, C., Mondal, M.,
1287 Mason, K., Elkhalifa, S., Smith, L.M.*, et al.* (2020). Discovery of a Potent and Selective Covalent Inhibitor
1288 and Activity-Based Probe for the Deubiquitylating Enzyme UCHL1, with Antifibrotic Activity. J Am
1289 Chem Soc *142*, 12020-12026.
1290 Panyain, N., Godinat, A., Thawani, A.R., Lachiondo-Ortega, S., Mason, K., Elkhalifa, S., Smith, L.M.,
1291 Harrigan, J.A., and Tate, E.W. (2021). Activity-based protein profiling reveals deubiquitinase and
1292 aldehyde dehydrogenase targets of a cyanopyrrolidine probe. RSC Med Chem *12*, 1935-1943.

Perez-Riverol, Y., Bai, J., Bandla, C., Garcia-Seisdedos, D., Hewapathirana, S., Kamatchinathan, S., Kundu, D.J., Prakash, A., Frericks-Zipper, A., Eisenacher, M.*, et al.* (2022). The PRIDE database resources in 2022: a hub for mass spectrometry-based proteomics evidences. Nucleic Acids Res *50*, D543-D552.

Py, B.F., Kim, M.S., Vakifahmetoglu-Norberg, H., and Yuan, J. (2013). Deubiquitination of NLRP3 by BRCC3 critically regulates inflammasome activity. Mol Cell *49*, 331-338.

Qin, W., Cho, K.F., Cavanagh, P.E., and Ting, A.Y. (2021). Deciphering molecular interactions by proximity labeling. Nat Methods *18*, 133-143.

Qu, Z., Zhou, J., Zhou, Y., Xie, Y., Jiang, Y., Wu, J., Luo, Z., Liu, G., Yin, L., and Zhang, X.L. (2020). Mycobacterial EST12 activates a RACK1-NLRP3-gasdermin D pyroptosis-IL-1beta immune pathway. Sci Adv *6*.

Ramachandran, A., Kumar, B., Waris, G., and Everly, D. (2021). Deubiquitination and Activation of the NLRP3 Inflammasome by UCHL5 in HCV-Infected Cells. Microbiol Spectr *9*, e0075521.

Ren, G., Zhang, X., Xiao, Y., Zhang, W., Wang, Y., Ma, W., Wang, X., Song, P., Lai, L., Chen, H.*, et al.* (2019). ABRO1 promotes NLRP3 inflammasome activation through regulation of NLRP3 deubiquitination. EMBO J *38*.

Samir, P., Kesavardhana, S., Patmore, D.M., Gingras, S., Malireddi, R.K.S., Karki, R., Guy, C.S., Briard, B., Place, D.E., Bhattacharya, A.*, et al.* (2019). DDX3X acts as a live-or-die checkpoint in stressed cells by regulating NLRP3 inflammasome. Nature *573*, 590-594.

Shao, B.Z., Xu, Z.Q., Han, B.Z., Su, D.F., and Liu, C. (2015). NLRP3 inflammasome and its inhibitors: a review. Front Pharmacol *6*, 262.

Sharif, H., Wang, L., Wang, W.L., Magupalli, V.G., Andreeva, L., Qiao, Q., Hauenstein, A.V., Wu, Z., Nunez, G., Mao, Y., and Wu, H. (2019). Structural mechanism for NEK7-licensed activation of NLRP3 inflammasome. Nature *570*, 338-343.

Song, A., Hazlett, Z., Abeykoon, D., Dortch, J., Dillon, A., Curtiss, J., Martinez, S.B., Hill, C.P., Yu, C., Huang, L.*, et al.* (2021). Branched ubiquitin chain binding and deubiquitination by UCH37 facilitate proteasome clearance of stress-induced inclusions. Elife *10*.

Song, H., Liu, B., Huai, W., Yu, Z., Wang, W., Zhao, J., Han, L., Jiang, G., Zhang, L., Gao, C., and Zhao, W. (2016). The E3 ubiquitin ligase TRIM31 attenuates NLRP3 inflammasome activation by promoting proteasomal degradation of NLRP3. Nat Commun *7*, 13727.

Song, H., Zhao, C., Yu, Z., Li, Q., Yan, R., Qin, Y., Jia, M., and Zhao, W. (2020). UAF1 deubiquitinase complexes facilitate NLRP3 inflammasome activation by promoting NLRP3 expression. Nat Commun *11*, 6042.

Stark, C., Breitkreutz, B.J., Reguly, T., Boucher, L., Breitkreutz, A., and Tyers, M. (2006). BioGRID: a general repository for interaction datasets. Nucleic Acids Res *34*, D535-539.

Swanson, K.V., Deng, M., and Ting, J.P. (2019). The NLRP3 inflammasome: molecular activation and regulation to therapeutics. Nat Rev Immunol *19*, 477-489.

Tang, J., Tu, S., Lin, G., Guo, H., Yan, C., Liu, Q., Huang, L., Tang, N., Xiao, Y., Pope, R.M.*, et al.* (2020). Sequential ubiquitination of NLRP3 by RNF125 and Cbl-b limits inflammasome activation and endotoxemia. J Exp Med *217*.

Teo, G., Liu, G., Zhang, J., Nesvizhskii, A.I., Gingras, A.C., and Choi, H. (2014). SAINTexpress: improvements and additional features in Significance Analysis of INTeractome software. J Proteomics *100*, 37-43.

van Wilgenburg, B., Browne, C., Vowles, J., and Cowley, S.A. (2013). Efficient, long term production of monocyte-derived macrophages from human pluripotent stem cells under partly-defined and fully-defined conditions. PLoS One *8*, e71098.

Vande Walle, L., Van Opdenbosch, N., Jacques, P., Fossoul, A., Verheugen, E., Vogel, P., Beyaert, R., Elewaut, D., Kanneganti, T.D., van Loo, G., and Lamkanfi, M. (2014). Negative regulation of the NLRP3 inflammasome by A20 protects against arthritis. Nature *512*, 69-73.

Vander Linden, R.T., Hemmis, C.W., Schmitt, B., Ndoja, A., Whitby, F.G., Robinson, H., Cohen, R.E., Yao, T., and Hill, C.P. (2015). Structural basis for the activation and inhibition of the UCH37 deubiquitylase. Mol Cell *57*, 901-911.

Vaughan-Jackson, A., Stodolak, S., Ebrahimi, K.H., Browne, C., Reardon, P.K., Pires, E., Gilbert-Jaramillo, J., Cowley, S.A., and James, W.S. (2021). Differentiation of human induced pluripotent stem cells to authentic macrophages using a defined, serum-free, open-source medium. Stem Cell Reports *16*, 1735-1748.

Vijayaraj, S.L., Feltham, R., Rashidi, M., Frank, D., Liu, Z., Simpson, D.S., Ebert, G., Vince, A., Herold, M.J., Kueh, A.*, et al.* (2021). The ubiquitylation of IL-1beta limits its cleavage by caspase-1 and targets it for proteasomal degradation. Nat Commun *12*, 2713.

Washer, S.J., Perez-Alcantara, M., Chen, Y., Steer, J., James, W.S., Trynka, G., Bassett, A.R., and Cowley, S.A. (2022). Single-cell transcriptomics defines an improved, validated monoculture protocol for differentiation of human iPSC to microglia. Sci Rep *12*, 19454.

Wu, T., Hu, E., Xu, S., Chen, M., Guo, P., Dai, Z., Feng, T., Zhou, L., Tang, W., Zhan, L.*, et al.* (2021). clusterProfiler 4.0: A universal enrichment tool for interpreting omics data. Innovation (Camb) *2*, 100141.

Xiang, Y., Li, X., Cai, M., and Cai, D. (2023). USP9X promotes lipopolysaccharide-stimulated acute lung injury by deubiquitination of NLRP3. Cell Biol Int *47*, 394-405.

Xiao, L., Magupalli, V.G., and Wu, H. (2023). Cryo-EM structures of the active NLRP3 inflammasome disc. Nature *613*, 595-600.

Xu, T., Yu, W., Fang, H., Wang, Z., Chi, Z., Guo, X., Jiang, D., Zhang, K., Chen, S., Li, M.*, et al.* (2022). Ubiquitination of NLRP3 by gp78/Insig-1 restrains NLRP3 inflammasome activation. Cell Death Differ *29*, 1582-1595.

Yan, Y., Jiang, W., Liu, L., Wang, X., Ding, C., Tian, Z., and Zhou, R. (2015). Dopamine controls systemic inflammation through inhibition of NLRP3 inflammasome. Cell *160*, 62-73.

Yang, X.D., Li, W., Zhang, S., Wu, D., Jiang, X., Tan, R., Niu, X., Wang, Q., Wu, X., Liu, Z.*, et al.* (2020). PLK4 deubiquitination by Spata2-CYLD suppresses NEK7-mediated NLRP3 inflammasome activation at the centrosome. EMBO J *39*, e102201.

Yu, G., Wang, L.G., Han, Y., and He, Q.Y. (2012). clusterProfiler: an R package for comparing biological themes among gene clusters. OMICS *16*, 284-287.

Zangiabadi, S., and Abdul-Sater, A.A. (2022). Regulation of the NLRP3 Inflammasome by Posttranslational Modifications. J Immunol *208*, 286-292.

Zhang, Z., Liu, N., Chen, X., Zhang, F., Kong, T., Tang, X., Yang, Q., Chen, W., Xiong, X., and Chen, X. (2021). UCHL1 regulates inflammation via MAPK and NF-kappaB pathways in LPS-activated macrophages. Cell Biol Int *45*, 2107-2117.

Zhang, Z.R., Meszaros, G., He, W.T., Xu, Y.F., Magliarelli, H.D., Mailly, L., Mihlan, M., Liu, Y.S., Gamez, M.P., Goginashvili, A.*, et al.* (2017). Protein kinase D at the Golgi controls NLRP3 inflammasome activation. Journal of Experimental Medicine *214*, 2671-2693.